

Multi-output calibration of a honeycomb seal via on-site surrogates

Jiangeng Huang* Robert B. Gramacy†

Abstract

We consider large-scale industrial computer model calibration, combining multi-output simulation with limited physical observation, involved in the development of a honeycomb seal. Toward that end, we adopt a localized sampling and emulation strategy called “on-site surrogates (OSSs)”, designed to cope with the amalgamated challenges of high-dimensional inputs, large-scale simulation campaigns, and nonstationary response surfaces. In previous applications, OSSs were one-at-a-time affairs for multiple outputs leading to dissonance in calibration efforts for a common parameter set across outputs for the honeycomb. We demonstrate that a principal-components representation, adapted from ordinary Gaussian process surrogate modeling to the OSS setting, can resolve this tension. With a two-pronged – optimization and fully Bayesian – approach, we show how pooled information across outputs can reduce uncertainty and enhance efficiency in calibrated parameters and prediction for the honeycomb relative to the previous, “data-poor” univariate analog.

Keywords: Bayesian calibration, multivariate analysis, computer experiment, hierarchical model, big data, surrogate modeling, uncertainty quantification

1 Introduction

Computer simulation experiments play an increasingly pivotal role in scientific inquiry. STEM training, cheap hardware, and robust numerical libraries have democratized simulation as a means of exploration of complex physical (e.g., Mehta et al., 2014), biological (e.g., Johnson, 2008), engineering/materials (e.g., Zhang et al., 2015), and economic phenomena (e.g., Kita et al., 2016), to provide a few representative examples. We are interested in the use of simulation in the development of a so-called *honeycomb seal*, a device integral to oil

*Genentech, Inc., South San Francisco, CA 94080 huang.jiangeng@gene.com; corresponding author

†Department of Statistics, Virginia Tech

and gas recovery, together with colleagues at Baker Hughes, a General Electric company (BHGE). The honeycomb experiment mirrors a common setup in engineering applications, leveraging a general purpose simulator called ISOTSEAL, a commercial spin-off of tools developed first at Texas A&M (Kleynhans and Childs, 1997).

Adapting a solver like ISOTSEAL to a particular application like BHGE’s honeycomb is a two-stage process. One first tailors configuration files to reflect the design and operational parameters/conditions of the particular instance under study. Inevitably some of these computer model settings are unknown (precisely enough) in the actual system, so there is interest in *calibrating* these parameters based on a limited physical/field experimentation campaign. Simulations, collected under a range of settings of both unknown *calibration parameters* and known *design inputs* characterizing operating conditions, can then be “matched” with analogs observed in the field, and their residuals can drive inference for the unknown settings, comprising the second stage.

Although there are several ways to operationalize that idea, the canonical setup in the computer experiments literature is due to Kennedy and O’Hagan (2001, KOH hereafter). At a high level, with details in Section 2, KOH couples two Gaussian processes (GPs) together – one as a surrogate for the computer model (e.g., ISOTSEAL), and another to capture bias and noise between simulation and field observation, to form a multivariate normal (MVN) marginal likelihood which can drive inference for all unknowns, including the calibration parameters. KOH offers a nice synthesis of information sources, but is susceptible to confounding (e.g., Brynjarsdóttir and O’Hagan, 2014; Tuo and Wu, 2016; Plumlee, 2017; Gu, 2019). More important for us, however, is that it is computationally daunting. Cubic matrix decompositions for MVNs involved in GP-based inference will severely limit the size of simulation campaigns that can be entertained (See Santner et al. (2018); Gramacy (2020)). Historically, computer simulation was cumbersome, limiting the size of campaigns. With increasing computing power, the speed and size of computer simulation are evolving.

The ISOTSEAL simulator is fast, so a big campaign is reasonable computationally, but not so fast nor steady enough that simulations can be used directly (forgoing the surrogate) in an otherwise KOH-style setting (Higdon et al., 2004). Meanwhile a large simulation campaign is essential to capture stark changes in dynamics, simulation artifacts, and other “features” common to modern numerical solvers. A flexible meta-modeling apparatus is essential in order to cope with large training data sizes, and to adapt to and/or smooth over (i.e., separate signal from) “noise”/artifacts in such settings. Huang et al. (2020) proposed one such approach based on *on-site surrogates* (OSSs), motivated specifically by ISOTSEAL and the BHGE honeycomb, but also vetted generically in benchmark exercises. Huang et al. showed how the KOH apparatus, and variations based on modularization (Liu et al., 2009) and maximization (Gramacy et al., 2015), could be adapted to work with OSSs.

Huang et al. explored a single output feature and honeycomb/ISOTSEAL output is multi-dimensional. Our BHGE collaborators are interested in at least four frequencies of outputs on four properties of the system (16 total). Section 3 demonstrates a not-uncommon situation when attempting to apply KOH separately for multiple outputs: inconsistent inference about calibration parameters across analyses, challenging downstream data synthesis, and ultimately poor prediction. Specifically to the honeycomb, the physical dynamics in play are complex, and the imposition of complete independence across property and frequency, together to with a paucity of field data observation, throws too much information away.

KOH has subsequently been extended to multi-output simulation and field experimentation (e.g. Higdon et al., 2008), but with ordinary GP surrogates. In this paper we detail the application of OSSs in that context, which is easier said than done. Although the basic ingredients are similar to Higdon et al., via principal component decompositions, their application is non-trivial in this setting and requires care in methodological development as well as implementation, as we provide. Following Huang et al. (2020), we take a two-pronged approach: first via thrifty marginalize–maximize calculations, rather than faithful KOH, then full Bayes with MCMC. The result is a multi-output, large-scale, computer

model calibration framework that – at least in the case of the honeycomb – is able to resolve stark multi-output calibration inconsistencies by making effective use of the (joint) information in all of the available simulation and field data. We wish to clarify that we do not offer a remedy to confounding issues sometimes faced by KOH, whether for single or multiple outputs. However for the honeycomb, we show that these may not be a first-order concern. Our efforts target computation: building a high-fidelity multi-output KOH apparatus via approximation that can cope with large simulation campaigns.

The remainder of paper is organized as follows. Section 2 begins with review of basics: KOH, GPs, etc. Honeycomb specifics and univariate OSS calibration in Section 3. Section 4 combines these building blocks for calibration with multivariate outputs via OSSs leveraging linear dependence across output frequency. Thrifty modular and fully Bayesian KOH are enumerated in turn. Section 5 combines across output property, and Section 6 demonstrates the impact on prediction down-stream. Section 7 concludes with a discussion.

2 Review of elements

We introduce KOH calibration via GPs, and extensions for scale and multivariate output.

2.1 Basics: calibration and surrogate modeling

Kennedy and O’Hagan (2001) described a univariate Bayesian calibration framework, combining field experimental observations $y^F(\mathbf{x})$, at a vector of input design variables \mathbf{x} , with computer simulations $y^M(\mathbf{x}, \mathbf{u}^*)$, under ideal or “true” calibration/tuning parameter(s) \mathbf{u}^* , through a discrepancy or bias correction $b(\mathbf{x})$, between simulation and field:

$$y^F(\mathbf{x}) = y^M(\mathbf{x}, \mathbf{u}^*) + b(\mathbf{x}) + \epsilon, \quad \epsilon \stackrel{\text{iid}}{\sim} \mathcal{N}(0, \sigma_\epsilon^2). \quad (1)$$

Modeling and inference commences via Gaussian processes (GP) priors on $y^M(\mathbf{x}, \mathbf{u}^*)$ and $b(\mathbf{x})$. GPs provide a flexible nonparametric (Bayesian) structure for smooth functional relationships between inputs \mathbf{x} and output $f(\mathbf{x})$, where any finite number N of evaluations follow a multivariate normal (MVN) distribution: $f(\mathbf{x}) \sim \mathcal{N}_N(\mu(\mathbf{x}), \Sigma(\mathbf{x}, \mathbf{x}'))$. Inference for any aspect of μ and Σ given training data $\mathbf{D}_N = (\mathbf{X}_N, \mathbf{y}_N)$ may be facilitated by likelihoods, i.e., MVN densities. Often in practice $\mu(\cdot) = 0$. MVN density/likelihood evaluation for aspects of Σ , which is usually based on inverse Euclidean distance up to several unknown hyperparameters ϕ , involve cubic-in- N matrix decomposition for inverses and determinants, which can be a bottleneck in large-scale applications.

This is exacerbated in the KOH setting where Eq. (1) implies a joint distribution for computer model training data $\mathbf{D}_N = (\mathbf{X}_N, \mathbf{y}_N)$ and field data $\mathbf{D}_F = (\mathbf{X}_F, \mathbf{y}_F)$:

$$\begin{bmatrix} \mathbf{y}_N \\ \mathbf{y}_F \end{bmatrix} \sim \mathcal{N}_{N+F}(\mathbf{0}, \Sigma(\mathbf{u})), \quad \text{where} \quad \Sigma(\mathbf{u}) \equiv \begin{bmatrix} \Sigma_N & \Sigma_{F,N}^\top(\mathbf{u}) \\ \Sigma_{F,N}(\mathbf{u}) & \Sigma_F(\mathbf{u}) + \Sigma_F^b \end{bmatrix}. \quad (2)$$

In (2) above, $\Sigma_N \equiv \Sigma([\mathbf{X}_N, \mathbf{U}_N])$ is an $N \times N$ covariance matrix for simulations $y^M(\cdot)$, capturing pairwise covariance between $p_x + p_u$ dimensional inputs (\mathbf{x}, \mathbf{u}) , and $\mathbf{U}_N \equiv [\mathbf{u}_1^\top, \dots, \mathbf{u}_N^\top]$ stacks N length p_u row vectors. The off-diagonal $\Sigma_{F,N}(\mathbf{u})$ is an $F \times N$ matrix capturing covariance between simulation inputs $[\mathbf{X}_N, \mathbf{U}_N]$ and field inputs $[\mathbf{X}_F, \mathbf{U}_F]$, again under $y^M(\cdot)$, where $\mathbf{U}_F \equiv [\mathbf{u}^\top, \dots, \mathbf{u}^\top]$ stacks F identical row vectors of (unknown) parameters \mathbf{u} . Similarly, $\Sigma_F(\mathbf{u}) \equiv \Sigma([\mathbf{X}_F, \mathbf{U}_F])$ is $F \times F$ for $[\mathbf{X}_F, \mathbf{U}_F]$, $y^M(\cdot)$ dynamics between field data observations. Lastly, Σ_F^b is an $F \times F$ matrix of covariances specified by the bias correction GP $b(\mathbf{x})$ acting only field inputs \mathbf{X}_F .

Fully Bayesian inference for unknown \mathbf{u} under prior $p(\mathbf{u})$ hinges on $p(\mathbf{y}_N, \mathbf{y}_F | \mathbf{u})$, the MVN (marginal) likelihood implied by Eq. (2). Computational challenges are evident in inverse $\Sigma^{-1}(\mathbf{u})$ and determinant $|\Sigma(\mathbf{u})|$ evaluations involved in such density evaluations. A single Cholesky decomposition could furnish both in $\mathcal{O}((N+F)^3)$ flops. However, notice

that not all blocks of $\Sigma(\mathbf{u})$ change as \mathbf{u} varies. While this implies potential for economies, the computational demands are still substantial (e.g., cubic in $N \gg F$) and nonetheless requires $\mathcal{O}((N + F)^2)$ for storage. For more details see Gramacy (2020, Section 8.1).

If computational hurdles can be surmounted, synthesis of information at varying fidelity (i.e., over field and simulation) can be a highly lucrative affair in spite of notorious identifiability challenges with remedies of coming in Bayesian (Higdon et al., 2004; Brynjarsdóttir and O’Hagan, 2014; Plumlee, 2017; Gu and Wang, 2018) and frequentist (Tuo and Wu, 2015, 2016; Wong et al., 2017; Plumlee, 2019) flavors. We do not, ourselves, wade into these waters, in part because these remedies can be at odds with computational tractability in modern big-data application (Marmin and Filippone, 2022). However *modularization* Liu et al. (2009), imposing partial independence on the joint MVN structure, separating surrogate $\hat{y}(\mathbf{x}, \mathbf{u})$ and bias $\hat{b}(\mathbf{x})$ fitting, can be both simple and effective.

2.2 Scaling up

For our purposes, a modular setup allows for thriftier surrogate modeling, and thus more tractable posterior inference for \mathbf{u} in large-data settings. Gramacy et al. (2015) leveraged modularization for a very large radiative shock hydrodynamics experiment via local approximate Gaussian processes (LAGP; Gramacy and Apley, 2015). LAGP uses a neighborhood of $n \ll N$ nearby data subsets for much faster inference.

$$\begin{aligned} \hat{\mathbf{y}}_N^M(\mathbf{X}_N^M, \mathbf{U}_N) &\longrightarrow \hat{\mathbf{y}}_n^M(\mathbf{X}_n^M, \mathbf{U}_n) \\ \text{Global GP} &\longrightarrow \text{laGP} \end{aligned} \tag{3}$$

Inference for \mathbf{u} proceeds via maximization of the posterior for $b(\cdot)$ through the observed discrepancy $\mathbf{D}_F^B(\mathbf{u}) = (\mathbf{X}_F, \mathbf{y}_F - \hat{\mathbf{y}}_F^M(\mathbf{u}))$:

$$\hat{\mathbf{u}} = \arg \max_{\mathbf{u}} \left\{ p(\mathbf{u}) \left[\max_{\phi_b} p_b(\phi_b \mid \mathbf{D}_F^B(\mathbf{u})) \right] \right\}, \tag{4}$$

where p_b is the MVN (marginal) likelihood for the GP prior on $b(\cdot)$, and ϕ_b are any hyper-parameters involved in the bias covariance structure, e.g., lengthscales.

Huang et al. (2020) developed on-site surrogates (OSSs), essentially pairing a design strategy with local GP surrogate modeling for KOH. Foreshadowing somewhat, as details are coming shortly in Section 3, they were motivated by the unique characteristics of (cheap/fast but erratic and high-dimensional) ISOTSEAL for the honeycomb. Compared to conventional simulators (slow but smooth and low-dimensional) the honeycomb demanded a large ISOTSEAL campaign of $N = 292,000$ runs to fully map out the response surface. Yet only a small handful $F = 292$ of field-data observations were available.

To resolve this “too big, too small” dilemma, Huang et al. proposed to design/fit ISOTSEAL simulations/surrogates “on-site” as follows: focus simulation designs, separately, on each of the physical experimental input sites \mathbf{x}_i , for $i = 1, 2, \dots, F$, paired with space-filling designs at calibration inputs \mathbf{u} of size $n_i = 1000$. Extending chart (3):

$$\begin{array}{ccccc} \hat{\mathbf{y}}_N^M(\mathbf{X}_N^M, \mathbf{U}_N) & \longrightarrow & \hat{\mathbf{y}}_n^M(\mathbf{X}_n^M, \mathbf{U}_n) & \longrightarrow & \hat{\mathbf{y}}_{n_i}^M(\mathbf{U}_{n_i}), i = 1, 2, \dots, F \\ \text{Global GP} & \longrightarrow & \text{laGP} & \longrightarrow & \text{OSSs} \end{array} \quad (5)$$

where n_i denotes the number of ISOTSEAL runs at the i^{th} site. In this way, the heavy $p_x + p_u = 17\text{d}$ simulation/emulation cargo is decomposed onto a handful (F) of lighter, individually focused $p_u = 4\text{d}$ sites. Consequently, OSSs address computational bottlenecks, provide non-stationary flexibility, automatically smooth over artifacts in some cases, and interpolates dynamics in others. Modularized calibration via maximization (4) for $\hat{\mathbf{u}}$ is straightforward. OSSs also create a highly sparse kernel for $\Sigma(\mathbf{u})$ in (2), so fully Bayesian KOH inference \mathbf{u} is tractable even with N in the millions.

2.3 Calibration with multivariate outputs

Although ideal for ISOTSEAL in many respects, this OSS strategy was for single-outputs. In Section 3.1 we show that separate application on honeycomb’s multiple outputs (varying frequencies and stiffness/damping coefficients) is problematic, motivating our main methodological contribution [Section 4]. Generally speaking, high dimensional simulation output can manifest in many ways: functional (Bayarri et al., 2007; Higdon et al., 2008), time series (Conti and O’Hagan, 2010; Fadikar et al., 2018), spatial (Bayarri et al., 2009), spatial-temporal (Gu and Berger, 2016), spectral (Guinness, 2019), with derivatives (McFarland et al., 2008). Besides being more complex, multivariate output naturally implies larger data size, aggravating computational challenges. Yet combining highly multivariate, physically meaningful information, offers the potential for improved posterior concentration and identification in calibration (see, e.g. Arendt et al., 2012; Jiang et al., 2016).

Dimension reduction, utilized appropriately, can help. For example, Higdon et al. (2008) extended univariate KOH into highly multivariate settings through principal components,

$$\mathbf{y}^F(\mathbf{x}) = \mathbf{K}^M \mathbf{w}^M(\mathbf{x}, \mathbf{u}^*) + \mathbf{K}^B \mathbf{w}^B(\mathbf{x}) + \epsilon. \quad (6)$$

In this framework, high dimensional field observations $\mathbf{y}^F(\mathbf{x})$ are modeled through $\mathbf{w}^M(\mathbf{x}, \mathbf{u}^*)$ via orthogonal basis matrix \mathbf{K}^M , and discrepancies $\mathbf{w}^B(\mathbf{x})$ via \mathbf{K}^B . Crucially, inference remains tractable via MCMC, at least compared to the single-output analog, and so long as training data sizes (N, F) are moderate. We aim to port this into the OSS framework [Section 4]. Other multi-output calibration approaches, which seem less well-matched to our honeycomb setting, include wavelet bases for functional outputs (Bayarri et al., 2007), and the linear model of co-regionalization (LMC; Paulo et al., 2012).

3 Honeycomb specifics

Centrifugal compressors employ seals to minimize leakage in gas compression phases, preventing back flow and consequently performance decay. Conventional annular gas seals, such as labyrinth and abrasible seals, cause gas recirculation around the shaft and produce destabilizing vibration effects. Honeycomb seals are used in high performance turbomachinery to promote stability via damping (see, e.g. Childs, 1993). Here we consider a honeycomb rotor stabilizing gas seal under development at BHGE.

The system under study is characterized by input–output relationships between variables representing seal geometry and flow dynamics. These include $p_x = 13$ controllable physical design inputs \mathbf{x} , including rotational speed, cell depth, seal diameter and length, inlet swirl, gas viscosity, gas temperature, compressibility factor, specific heat, inlet/outlet pressure, and inlet/outlet clearance. The field experiment, from BHGE’s component-level honeycomb seal test campaign, comprises $F = 292$ runs varying a subset of those conditions, \mathbf{X}_F , believed to have greatest variability during turbomachinery operation: clearance, swirl, cell depth, seal length, and seal diameter. Measured output features include direct/cross stiffness and damping properties at multiple frequencies.

A general-purpose rotordynamic simulator called ISOTSEAL, built upon bulk-flow theory, virtually stress seals like the honeycomb. First developed at Texas A&M University (Kleynhans and Childs, 1997), it offers fast evaluation (usually about one second) of gas seal force coefficients. Our BHGE colleagues developed an R interface mapping the seventeen scalar inputs for the honeycomb into the format required for ISOTSEAL. Thirteen of those inputs match up with the columns of \mathbf{X}_F (i.e., they are \mathbf{x} ’s); four are calibration parameters \mathbf{u} , which could not be controlled in the field. These comprise statoric and rotoric friction coefficients n_s, n_r and exponents m_s, m_r . We work with friction factors coded to the unit cube: $(n_s, m_s, n_r, m_r)^\top \rightarrow (u_1, u_2, u_3, u_4)^\top \in [0, 1]^4$, primarily to protect BHGE’s intellectual property. Throughout, we follow Huang et al. (2020) and use independent Beta(2, 2)

priors on (u_1, u_2, u_3, u_4) to nudge the posterior toward the interior of the space. However, we comment briefly on a limited sensitivity analysis in Section 5.2.

3.1 Multivariate outputs

The potential set of output features that could be monitored for the honeycomb seal are many. Here we focus on four rotordynamic coefficients, or properties: direct stiffness (K_d), cross stiffness (k_c), direct damping (C_d), and cross damping (c_c), measured at the following frequencies: 28, 70, 126, and 154 Hz; so 16 outputs in total. These are our \mathbf{y} -values, measured either in the field as \mathbf{y}_i^F , collected as \mathbf{Y}_F , or as \mathbf{y}_i^M simulated via ISOTSEAL, collected as \mathbf{Y}_N . Huang et al. (2020) only considered one of these: K_d at 28 Hz.

The turbomachinery literature and bulk-flow theory (Hirs, 1973) provides some insight into the relationship between these four properties. For example, D’Souza and Childs (2002) demonstrate that classical transfer for a honeycomb gas seal process can be expressed in a conventional linear motion/reaction-force model

$$-\begin{bmatrix} F_x \\ F_y \end{bmatrix} = \begin{bmatrix} K_d & k_c \\ -k_c & K_d \end{bmatrix} \begin{bmatrix} x \\ y \end{bmatrix} + \begin{bmatrix} C_d & c_c \\ -c_c & C_d \end{bmatrix} \begin{bmatrix} \dot{x} \\ \dot{y} \end{bmatrix} \quad (\text{units omitted}). \quad (7)$$

Direct stiffness K_d and damping C_d account for orthogonal reaction forces in x and y axes. Cross-coupled stiffness k_c and damping c_c describe reaction orthogonal to directions of motion. Other mechanical engineering studies of rotordynamic coefficients include Childs (1993); Kleynhans and Childs (1997); Delgado et al. (2012).

To access simulated versions of these outputs we augmented BHGE’s R interface for

ISOTSEAL and then re-ran the campaign of Huang et al. (2020), collecting following:

$$\hat{\mathbf{Y}}^M(\mathbf{x}, \mathbf{u}) \equiv \hat{y}_{ijk}^M(\mathbf{u}), \quad \text{for } \begin{cases} i = 1, 2, \dots, F \text{ (i.e., each field data pair)} \\ j \in \{1, 2, 3, 4\} \text{ coding properties } \{K_d, k_c, C_d, c_c\} \\ k \in \{1, 2, 3, 4\} \text{ coding frequencies.} \end{cases} \quad (8)$$

In total this involved $292 \times 1000 \times 4 \approx 1,168,000$ ISOTSEAL runs. Each run at inputs (\mathbf{x}, \mathbf{u}) is for a single output frequency, producing all four rotordynamic coefficients simultaneously. In about 2% of cases a convergence issue is detected, terminating with an NA-coded missing value after about three seconds. Collecting all 4,672,000 measurements, over the four frequencies, took about three days when divided up across several multi-core compute nodes. Our experiment resulted in $N = \sum_{i=1}^F n_i = 286,282$ successfully terminated runs, with most sites (241 out of 292) having a full $n_i = 1,000$. Of the 51 with missing responses of varying multitudes, the smallest was $n_{238} = 574$. In total, we collected $16 \times 286,282 = 4,580,512$ on-site multivariate ISOTSEAL runs. The missingness pattern is similar to that reported in Huang et al. (2020), even across output coefficients and frequencies because a failed run at a particular input affects all outputs equally. One of the aims of OSS calibration is to extrapolate to these unknown/missing parameter regions after calibrating to field data. See, e.g., Marcy and Storlie (2020), albeit on a somewhat smaller scale.

A 16-fold increase in data, exhibiting all of the features of the single-output case (non-stationarity, missingness, etc.), demands a scale-up of OSS calibration in several directions. We describe that in Section 4, but it shares pre-processing with a separate analysis of each output. We therefore turn first to a description of that simpler process, which ultimately serves as a straw man against our fully multivariate analysis.

3.2 Separate univariate analysis

Consider OSSs built separately for each of the outputs. Each OSS comprises a fitted GP between successful on-site ISOTSEAL run outputs y_{ijk}^M at \mathbf{x}_i and with novel 1,000-element maximin Latin hypercube sample (LHS; Morris and Mitchell, 1995) \mathbf{U}_{ijk} , for fixed j and k . Specifically, \hat{y}_{ijk}^M is built by fitting a stationary zero-mean GP using a scaled and nugget-augmented separable Gaussian kernel trained only on the space of parameter \mathbf{u} ,

$$\Sigma_{ijk}(\mathbf{u}_{jk}, \mathbf{u}'_{jk}) = \tau_{ijk}^2 \left\{ \exp \left[- \sum_{l=1}^{p_u} \frac{\|\mathbf{u}_{ijkl} - \mathbf{u}'_{ijkl}\|^2}{\theta_{ijkl}} \right] + \delta_{u,u'} \eta_{ijk} \right\}, \quad (9)$$

where $\delta_{u,u'}$ is the Kronecker delta, τ_{ijk}^2 is a scale parameter, $\boldsymbol{\theta}_{ijk} = (\theta_{ijk1}, \theta_{ijk2}, \dots, \theta_{ijkp_u})^\top$ a vector of lengthscales, and η_{ijk} is a nugget – all being specific to the i^{th} site, j^{th} output, and k^{th} frequency. Denote the set of hyperparameters of the ijk^{th} OSS as $\boldsymbol{\phi}_{ijk} = \{\tau_{ijk}^2, \boldsymbol{\theta}_{ijk}, \eta_{ijk}\}$, with indices following Eq. (8).

To offer some visual contrast between these fits, Figure 1 shows the site-wise noise level $\hat{\tau}_{ijk}^2 \hat{\eta}_{ijk}$ across the $F = 292$ sites for the sixteen outputs. These are clearly non-constant, a testament to the nonstationary nature of OSSs across the input space represented by the 292 \mathbf{x}_i settings, but also highly consistent across outputs at each frequency level. This suggests that a certain amount of information in each frequency is redundant. Although somewhat less obvious at first glance, notice that the overall noise level decreases as the frequency increases. The amount by which noise level drops depends on the input location, suggesting there is novel information in each output frequency, which might manifest as spatial dependency, albeit in a large ($p_x = 17\text{d}$) space.

Before inserting these $292 \times 16 = 4,672$ OSSs into the KOH apparatus for calibration, we performed a hyperparameter stability and predictive accuracy check on a commensurately sized out-of-sample on-site testing data set, again sixteen-fold across 4,672,000 ISOTSEAL runs. The hyperparameters looked similar to Figure 1, and are not shown here to save space. Prediction accuracies are summarized in Figure 2. Each boxplot collects the 292

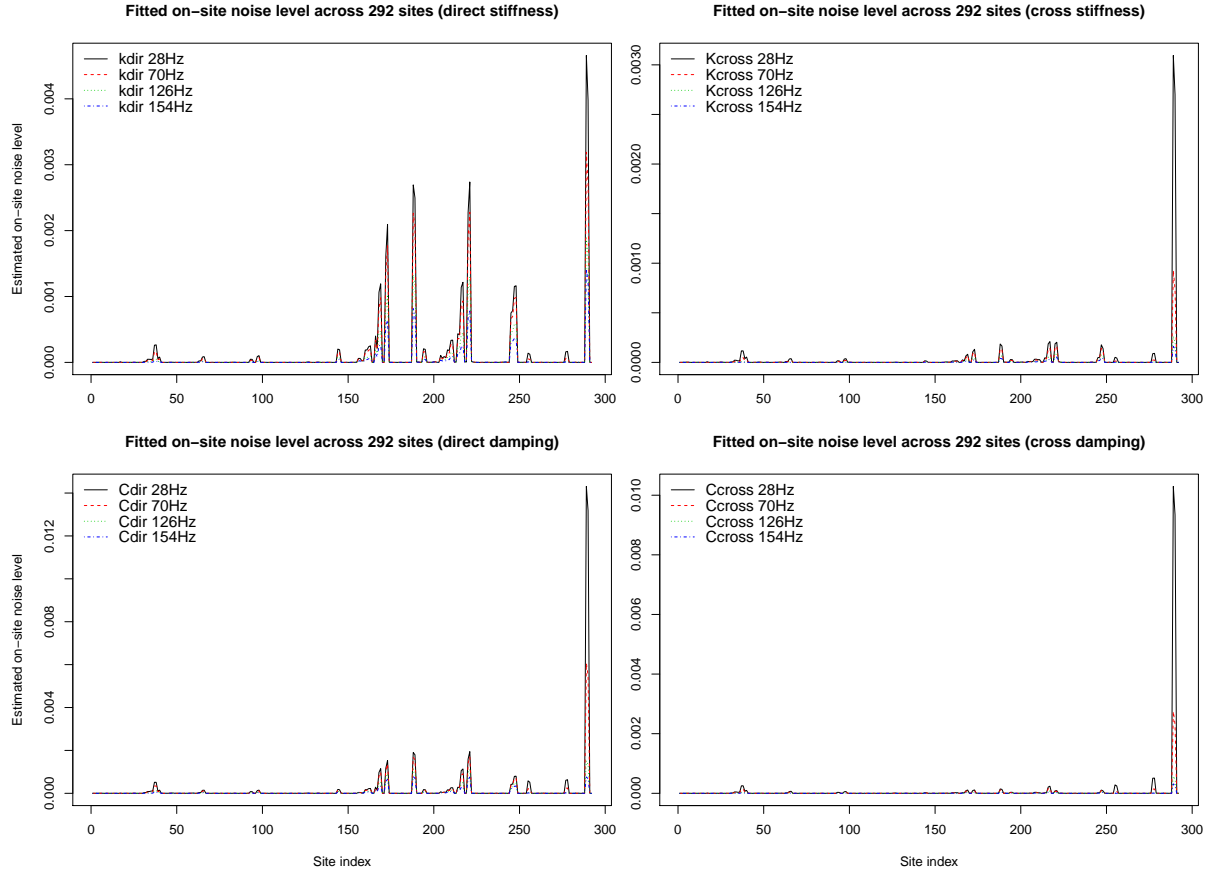


Figure 1: Univariate OSS noise levels represented by the trained $\hat{\tau}_{ijk}^2 \hat{\eta}_{ijk}$ for direct/cross stiffness and damping at each of the four frequencies.

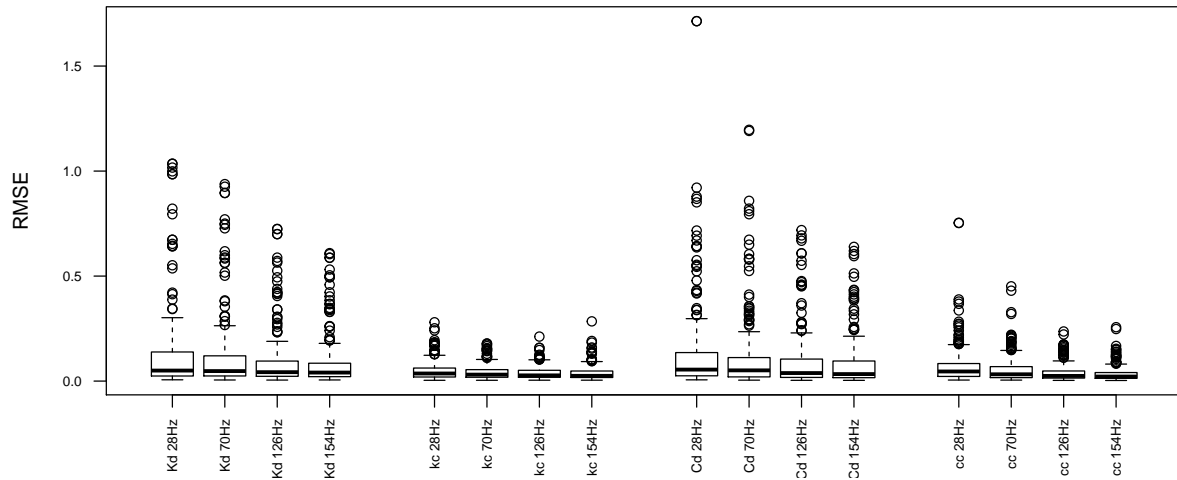


Figure 2: Boxplots of 292 out-of-sample root mean-squared errors (RMSEs).

on-site root mean-squared errors (RMSEs) from the $n_{ijk} \approx 1,000$ converged runs on site i , separately for output j and frequency k . Observe that most OSSs ($> 50\%$ via the median lines in the boxplots) act as interpolators on the sites, giving RMSEs are close to zero. The rest act as extrapolators or smoothers, with a small handful ($\approx 5\%$ outside the whiskers) extremely so. Also notice that the scales of RMSEs consistently decrease as frequency increases, coinciding with the in-sample pattern(s) observed in Figure 1.

3.3 Challenges from univariate OSSs calibration

Next, combining with field data, we performed separate OSS-based fully Bayesian calibrations for \mathbf{u} , repeating the Huang et al. univariate approach for each output and frequency. That is, we performed $4 \times 4 = 16$ MCMCs, 100,000 samples each, and discarded 5,000 as burn-in. Each MCMC run took about three days to finish, after a warm start from modular optimization (4). To demonstrate the drawbacks from this univariate approach, Figures 3 and 4 present two views into the posteriors for \mathbf{u}_{jk} .

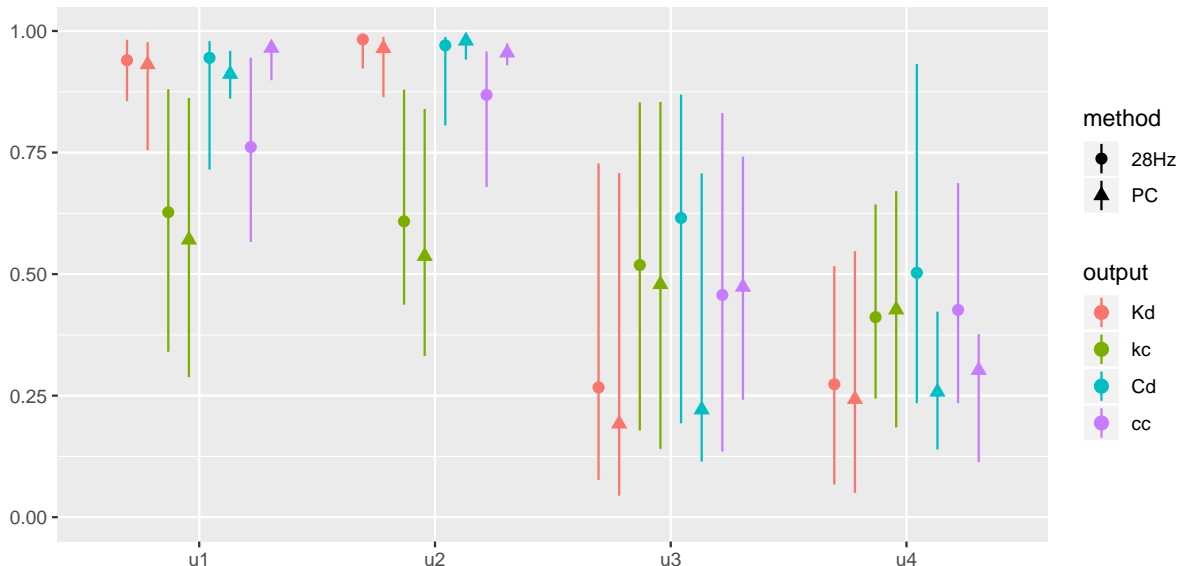


Figure 3: Marginal posterior distributions of \mathbf{u} from outputs K_d, k_c, C_d , and c_c at 28Hz (circles) and via principal components combining all output frequencies (triangles, Section 4.3). Dots indicate MAP values and error bars form 90% credible intervals.

Figure 3 shows marginal posteriors for the components of \mathbf{u}_{jk} for each output at 28Hz

($k = 1$). The other frequencies, provided in Supplement A.1, look similar. To support a comparison coming later in Section 4.3, the plot also shows results combining all frequencies which will be discussed in due course. Focusing on the 28Hz results, notice that while some coordinates, like u_3 and u_4 , exhibit consistency in the high overlap of their credible intervals, others like u_1 and u_2 do not. There would appear to be complimentary (unused) information in these independent analyses. For a slightly higher resolution view, Figure 4

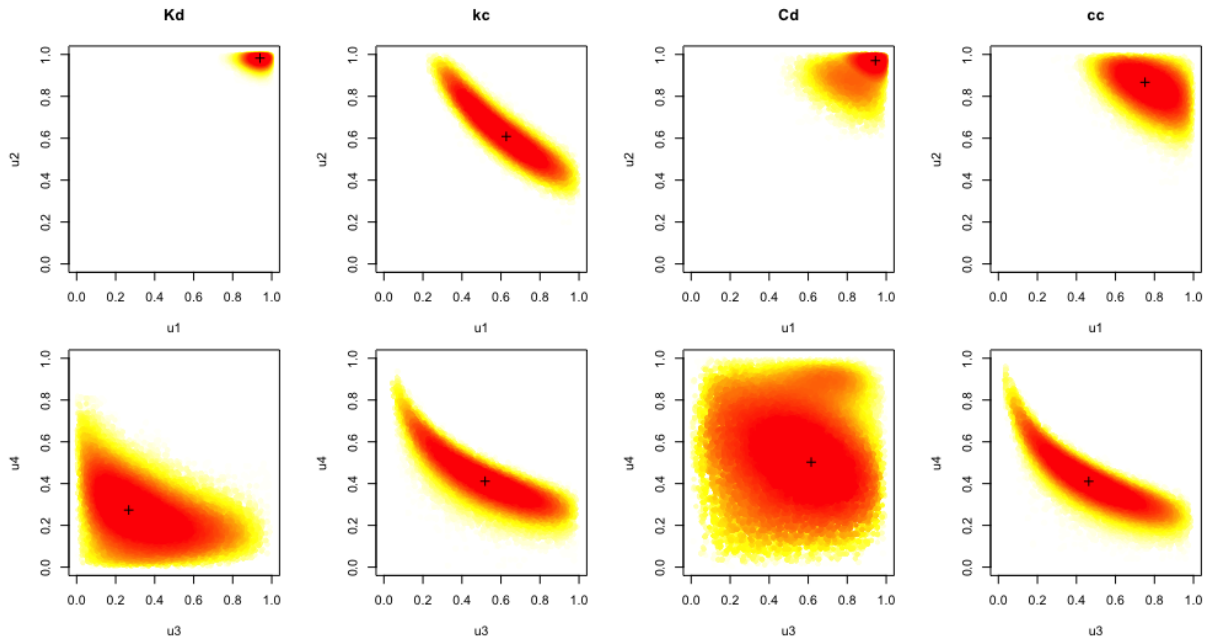


Figure 4: Bivariate marginal plots of single-output posterior samples of \mathbf{u} from outputs $K_d, k_c, C_d,$ and c_c at 28 Hz. Dots are 100,000 MCMC samples of \mathbf{u} , heat colored according to the rank of (log) posterior probability. The “+” indicates the MAP values.

shows posteriors for pairs $u_1 \times u_2$ for each output (at 28Hz) across the top, and $u_3 \times u_4$ across the bottom. Again, the set of similar visuals is completed in the supplemental material. In the top row, k_c stands out as the exception. Despite wider credible regions in the bottom row, only one pair (k_c, c_c) among the six resemble one another.

Taken together – and even for just these four sets of \mathbf{u}_{jk} posteriors, ignoring the other output frequencies – there is no way to stack them together in the 4-dimensional space to generate one single, concentrated solution with appropriate evaluation of individual param-

eter uncertainty from different outputs. These separately sampled \mathbf{u}_{jk} posteriors indicate heterogeneity in parameter learning with varied amount of uncertainty, creating more uncertainty downstream to any engineering decision-making. A joint analysis not only holds the potential to reconcile (at times) contradictory information, but would also drastically simplify downstream decision-making with far fewer posterior views to scrutinize.

4 On-site surrogates with basis representation

The essential insight behind OSS-based calibration is that learning for \mathbf{u} is primarily driven by model discrepancy $b(\mathbf{x})$, which can only be observed at field input sites \mathbf{X}_F , through residuals. At a conceptual level, extending that to multivariate output means evaluating vectors of outputs: $\mathbf{y}_{ijk}^F(\mathbf{X}_F)$ in the field and $\hat{\mathbf{y}}_{ijk}^M(\mathbf{X}_F, \mathbf{U}_i)$ for the surrogate, and then calculating discrepancies with extra indices.

$$\mathbf{y}_{ijk}^F(\mathbf{X}_F) - \hat{\mathbf{y}}_{ijk}^M(\mathbf{X}_F, \mathbf{U}_i), \quad i = 1, 2, \dots, F, \quad j = 1, 2, \dots, J, \quad k = 1, 2, \dots, K, \quad (10)$$

where \mathbf{U}_i is the design matrix (maximim LHS) of calibration parameter \mathbf{u} for converged n_i on-site runs for the i^{th} site. As with univariate outputs, as long as the surrogate is good at those locations, which OSSs facilitate, further considerations can be pushed downstream. For example, when new locations are of interest, say for prediction, new OSSs/runs can be built/performed there, which is trivial if (like ISOTSEAL) the simulations are fast.

The devil is, however, in the details for how these residuals (10) are modeled. Section 3.3 demonstrates that separating over j and k for the honeycomb leads to pathologies. Here we begin the description for a joint analysis, building a fitted bias for residuals all at once, to resolve those inconsistencies while ensuring that all relevant information is incorporated in posterior inference for \mathbf{u} , thus filtering to downstream tasks like prediction. What we propose below is customized, to a degree, to the honeycomb setting, e.g., via fixed j (output

classes) and pooling over k (output frequencies) in Eq. (10). Completing the description by combining over output classes (pooling over j) is deferred to Section 5. We begin here with some notational setup that applies for all j and k , and then fix j for the remainder of the section. Although we believe other applications – perhaps with more or fewer indices – could be set similarly, further speculation is left to Section 7.

Let $\mathbf{Y}_i^M(\mathbf{U}) = [\mathbf{y}_{i11}^M(\mathbf{U}_i), \mathbf{y}_{i12}^M(\mathbf{U}_i), \dots, \mathbf{y}_{i44}^M(\mathbf{U}_i)]$, for $i = 1, 2, \dots, F$, be a 16-column matrix (four outputs at four frequencies) holding the $n_i \approx 1000$ rows of converged ISOTSEAL runs for the i^{th} site. Now collect $F = 292$ of these $\mathbf{Y}_i^M(\mathbf{U}) = [\mathbf{Y}_1^M(\mathbf{U})^\top, \dots, \mathbf{Y}_F^M(\mathbf{U})^\top]^\top$

$$\mathbf{Y}^M(\mathbf{U}) = \begin{bmatrix} \mathbf{y}_{111}^M(\mathbf{U}_1) & \dots & \mathbf{y}_{144}^M(\mathbf{U}_1) \\ \vdots & \ddots & \vdots \\ \mathbf{y}_{F11}^M(\mathbf{U}_F) & \dots & \mathbf{y}_{F44}^M(\mathbf{U}_F) \end{bmatrix}_{N \times 16} \quad (11)$$

whose row dimension is $N = \sum_{i=1}^F n_i = 286,282$. Recall that \mathbf{U}_i are $n_i \times p_u$ on-site (maximin LHS) design matrices.

We performed an initial exploratory data analysis (EDA) with these data, one aspect of which is $\mathbf{Cor}\{\mathbf{Y}^M(\mathbf{U})\}$, visualized in Figure 5. Correlation strength and association is indicated numerically in the lower-triangle, by elliptical shape and direction in the upper half, and by color and shading in both. Four-by-four blocks are clearly evident in this view, indicating strong linear correlation between different frequency levels within the same property (block of) output, but weaker correlation between types. Our EDA also revealed similar correlations exhibited by the output-combined field data \mathbf{Y}^F , defined similarly. This is not shown here for brevity. Taken together, we conclude that parsimonious representation of across-frequency information could be beneficial to a joint modeling enterprise.

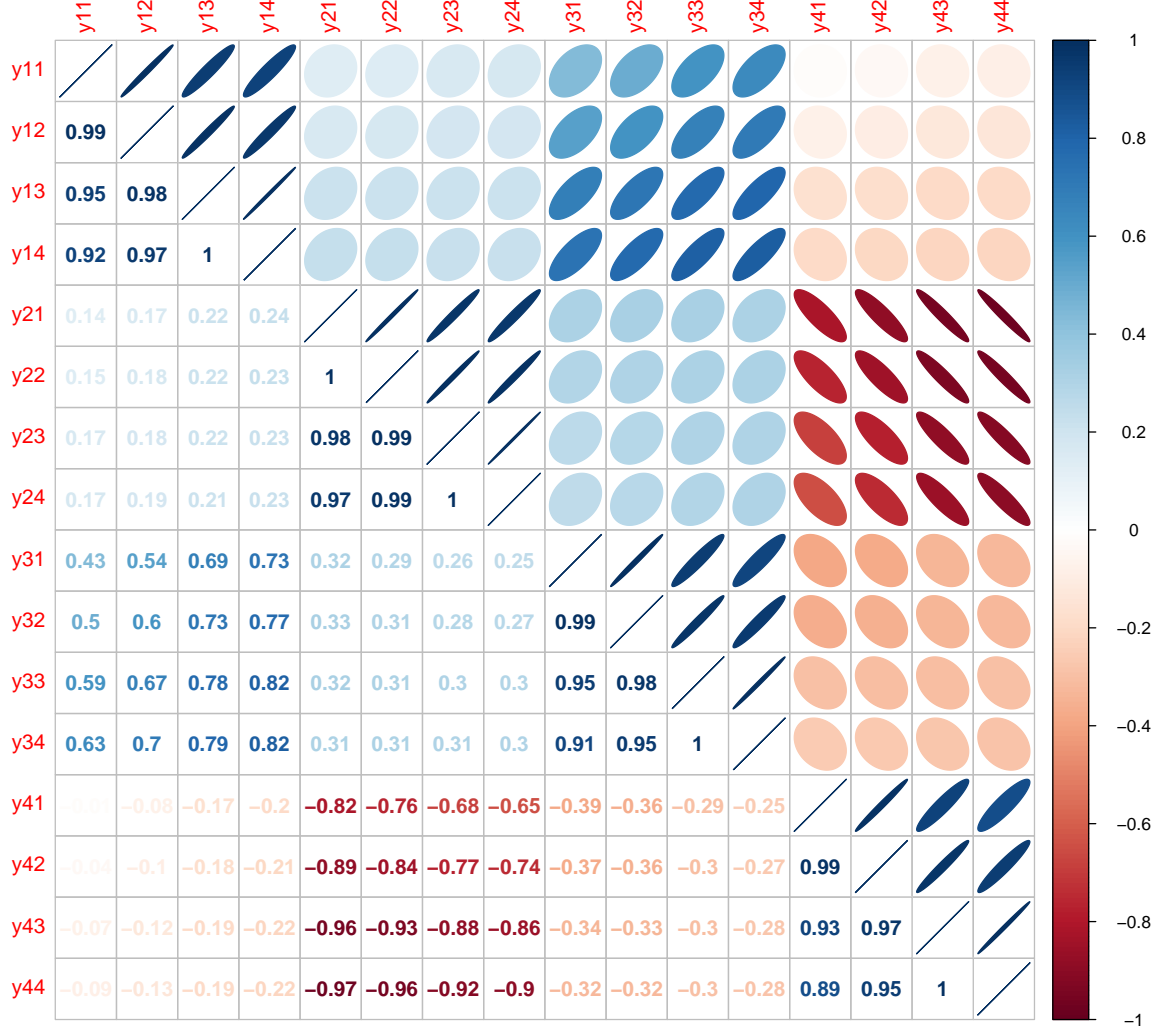


Figure 5: Correlation matrix (number in lower triangle and ellipse in upper triangle) of $N = 286,282$ multivariate ISOTSEAL simulation of direct/cross stiffness and damping at frequencies 28, 70, 126, and 154 Hz. In the output labels y_{jk} , $j = 1, \dots, 4$ for output property and $k = 1, \dots, 4$ for frequency, as defined in Eq. (8).

4.1 Principal component OSSs

We propose performing principal component analysis (PCA) across frequency outputs in an “on-site” fashion, i.e., fit a PC basis in the subspace spanned by $\mathbf{U}_i, i = 1, \dots, F$ on the F observed physical sites \mathbf{X}_F for each type (block, indexed by j) of outputs. Fixing j , we first center and standardize the correlated $K = 4$ frequencies, perform PCA on the $N \times K$

dimensional “on-site” matrix,

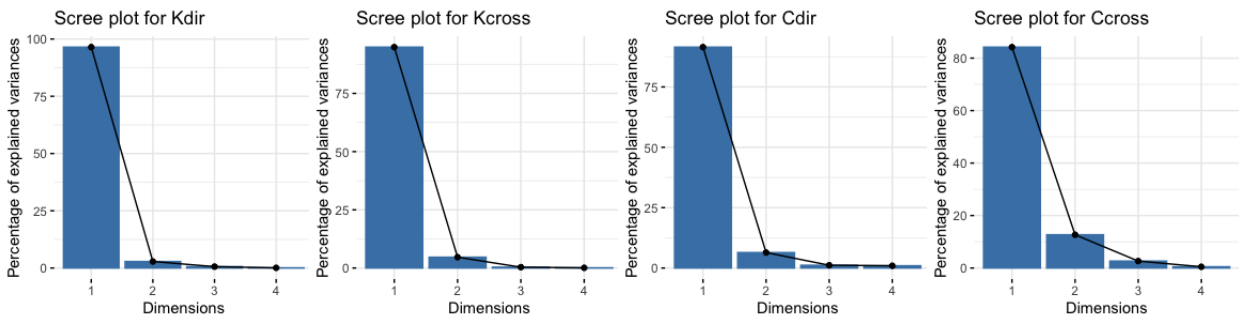
$$\text{PC}\{\mathbf{Y}_j^F - \mathbf{Y}_j^M\}, \quad \text{yielding eigenvectors } \mathbf{W}_j, \quad \text{for } j = 1, \dots, J. \quad (12)$$

In Eq. (12), \mathbf{Y}_j^F collects $K = 4$ columns of n_i -row replicated field outputs across frequencies,

$$\mathbf{Y}_j^F = \begin{bmatrix} \mathbf{y}_{1j1}^F & \cdots & \mathbf{y}_{1j4}^F \\ \vdots & \ddots & \vdots \\ \mathbf{y}_{Fj1}^F & \cdots & \mathbf{y}_{Fj4}^F \end{bmatrix}_{N \times 4}, \quad (13)$$

where $\mathbf{y}_{ijk}^F \equiv (y_{ijk}^F(\mathbf{x}_i), \dots, y_{ijk}^F(\mathbf{x}_i))^\top$ is the n_i -time duplicated field output $y_{ijk}^F(\mathbf{x}_i)$ on i^{th} site for output j at frequency k . Similarly, \mathbf{Y}_j^M collects $K = 4$ columns of on-site ISOTSEAL simulations on F sites at multiple frequencies provided in Eq. (11).

For honeycomb, there are $J = 4$ properties (blocks): $\{K_d, k_c, C_d, c_c\}$. Thus, we performed four separate PCAs in total. Figure 6 summarizes these via scree plots of variance decomposition, accompanied by a table with a numerical summary via the top variances. Notice that the first-PCs dominate in all four cases. Output c_c which might



Observed discrepancy on output	K_d	k_c	C_d	c_c
Variation represented in the first-PC	96.46%	94.89%	91.49%	84.19%
Variation represented in the second-PC	2.84%	4.66%	6.41%	12.68%

Figure 6: Scree plots and tabulation of PCA variances.

marginally benefit from the second principal direction.

This suggests that a Higdon et al. (2008)-style basis-based-surrogate (6), projecting

down to one principal direction for these four outputs (separately over output property j) could be effective here, after upgrading to accommodate OSSs. Instead of breaking down the simulator and discrepancies into two separate principal representations in (6), we prefer a single PCA through the matrix of eigenvectors \mathbf{W}_j trained from the whole “on-site” observed discrepancy in (12). In particular, we use the first (column) eigenvector \mathbf{w}_j^1 of \mathbf{W}_j to extract the first-PCs from multiple frequency outputs of both simulated $\mathbf{y}_j^{M1} = \mathbf{Y}_j^M \mathbf{w}_j^1$ and field $\mathbf{y}_j^{F1} = \mathbf{Y}_j^F \mathbf{w}_j^1$. Once extracted, we can put them together as

$$\mathbf{y}_j^{F1}(\mathbf{x}) = \mathbf{y}_j^{M1}(\mathbf{x}, \mathbf{u}^{*1}) + \mathbf{b}_j^1(\mathbf{x}) + \epsilon_j^1. \quad (14)$$

which may be interpreted as ordinary KOH in the first-PC subspace. Observe the introduction of new notation for model discrepancy $\mathbf{b}_j^1(\mathbf{x})$, best calibration setting \mathbf{u}^{*1} , and iid noise ϵ_j^1 , to recognize PC pre-processing to form $\mathbf{y}_j^{F1}(\mathbf{x})$ and \mathbf{y}_j^{M1} . Focus remains on observed sites only, i.e., $\mathbf{x} \equiv \mathbf{X}_F$ in the on-site setting, for observed discrepancies, and surrogate(s) trained on $N = 286,282$ dense paired with space-filling \mathbf{U}_i ’s. After learning, prediction, etc., may be linearly back-transformed to the original full space.

4.2 PC-level OSSs calibration: optimization and full Bayes

Each first on-site PC can be used in a separate calibration: four this time instead of sixteen in Section 3.3. Here we illustrate how these may plugged into the OSS calibration framework as an intermediate step toward a fully joint model in Section 5.

Modular calibration via optimization. Here the goal is to search for $\hat{\mathbf{u}}_j^1$ by maximizing the posterior probability of (observed) model discrepancy (4) in the first principal direction. Update Eq. (4) by swapping the univariate (column vector) observed discrepancy with that

based on first eigenvector \mathbf{w}_j^1 obtained in Eq. (12). I.e., for each of $j = 1, \dots, J$,

$$\mathbf{D}_F^B(\mathbf{u}) = (\mathbf{X}_F, \mathbf{y}_F - \hat{\mathbf{y}}_F^M(\mathbf{u})) \rightarrow \mathbf{D}_F^{j1}(\mathbf{u}_j^1) = (\mathbf{X}_F, (\mathbf{Y}_j^F - \hat{\mathbf{Y}}_j^M(\mathbf{u}_j^1))\mathbf{w}_j^1), \quad (15)$$

In (15), \mathbf{Y}_j^F is fixed and $\hat{\mathbf{Y}}_j^M(\mathbf{u}_j^1)$ are OSS [fitted as in Section 3.2] evaluations at \mathbf{u}_j^1 , which would vary along a numerical optimizer’s search trajectory. The mathematical programs are identical to Eq. (4) but with $\mathbf{D}_F^B(\mathbf{u}) \rightarrow \mathbf{D}_F^{j1}(\mathbf{u}_j^1)$ and $\phi \rightarrow \phi_j^1$ denoting hyperparameters involved in each of j GP-based (separable squared exponential) fitted discrepancies.

Bayesian joint inference. Posterior sampling of \mathbf{u}_j^1 requires projecting \mathbf{Y}_j^F (13) and \mathbf{Y}_j^M (11) onto their first principal axis, \mathbf{y}_j^{F1} and \mathbf{y}_j^{M1} respectively, via Eq. (12). Then, following Eq. (14), one may impose a joint MVN (2), with mean zero and covariance $\Sigma_j^1(\mathbf{u}_j^1)$, whose structure is re-notated below with appropriate indices/first-PC indicators:

$$\Sigma_j^1(\mathbf{u}_j^1) \equiv \begin{bmatrix} \Sigma_N^{j1} & \Sigma_{F,N}^{j1}(\mathbf{u}_j^1)^\top \\ \Sigma_{F,N}^{j1}(\mathbf{u}_j^1) & \Sigma_F^{j1}(\mathbf{u}_j^1) + \Sigma_b^{j1} \end{bmatrix}. \quad (16)$$

Posterior evaluation for \mathbf{u}_j^1 in a Metropolis setting requires decomposing this $\Sigma_j^1(\mathbf{u}_j^1)$ for inverse and determinant components of the MVN log likelihood. Note the size of this matrix is $(N + F)^2$, where $N + F = 286,574$ for our honeycomb application. Consequently, ordinary cubic in $(N + F)$ decomposition costs pose a serious bottleneck.

Fortunately, $\Sigma_j^1(\mathbf{u}_j^1)$ has a convenient structured-sparsity form under OSSs. The largest block Σ_N^{j1} , corresponding to the OSSs themselves, is the most sparse. It is block-diagonal with F blocks: $\Sigma_N^{j1} = \text{Diag}[\Sigma_i^{j1}(\mathbf{U}_i, \mathbf{U}_i)]$. Each block $\Sigma_i^{j1}(\mathbf{U}_i, \mathbf{U}_i)$ may be built from the kernel of the i^{th} OSS conditioned on any fitted hyperparameters from \mathbf{y}_{ij}^{M1} . Since it does not depend on \mathbf{u}_j^1 , each may be pre-decomposed separately at manageable $\mathcal{O}(n_i^3)$ cost.

The rest of $\Sigma_j^1(\mathbf{u}_j^1)$ requires bespoke construction given novel \mathbf{u}_j^1 , but still has convenient block-sparse structure. The simulator-field cross covariance piece is block-diagonal,

$\Sigma_{F,N}^{j1}(\mathbf{u}_j^1) = \text{Diag}[\Sigma_i^{j1}(\mathbf{u}_j^1, \mathbf{U}_i)]$, where $\Sigma_i^{j1}(\mathbf{u}_j^1, \mathbf{U}_i)$ is a row vector of site-wise covariance between calibration inputs \mathbf{u}_j^1 and on-site design matrix \mathbf{U}_i . Finally, although $\Sigma_F^{j1}(\mathbf{u}_j^1) + \Sigma_b^{j1}$ is dense, it is small ($F \times F$) and thus cheap to decompose. The first component $\Sigma_F^{j1}(\mathbf{u}_j^1)$ is block diagonal, where each block is like $\Sigma_i^j(\mathbf{U}_i, \mathbf{U}_i)$ from the i^{th} OSS kernel, except with a stacked \mathbf{u}_j^1 vectors in lieu of the \mathbf{U}_i . The second component Σ_b^{j1} is dense and comes from the discrepancy kernel using all field-data inputs. Any hyperparameters, e.g., $\hat{\phi}_j^1$ are most easily set via maximization-based pre-analysis, e.g., following Eq. (15), but could also be included in the MCMC. For consistency, zero-mean separable GPs are fitted for $\hat{\phi}_j^1$.

Once $\Sigma_j^1(\mathbf{u}_j^1)$ in Eq. (16) is built, for each proposed \mathbf{u}_j^1 setting in a Metropolis scheme, and after its component parts have been decomposed, a full decomposition – i.e., combining from constituent parts – involves tedious but ultimately straightforward matrix multiplication via partition inverse and determinant equations (e.g., Petersen and Pedersen, 2008) leveraging the multiple-OSSs setup,

$$\Sigma_j^1(\mathbf{u}_j^1)^{-1} = \begin{bmatrix} (\Sigma_N^{j1})^{-1} + (\Sigma_N^{j1})^{-1} \Sigma_{F,N}^{j1}(\mathbf{u}_j^1)^\top \mathbf{C}^{-1}(\mathbf{u}_j^1) \Sigma_{F,N}^{j1}(\mathbf{u}_j^1) (\Sigma_N^{j1})^{-1} & (\cdot)^\top \\ -\mathbf{C}^{-1}(\mathbf{u}_j^1) \Sigma_{F,N}^{j1}(\mathbf{u}_j^1) (\Sigma_N^{j1})^{-1} & \mathbf{C}^{-1}(\mathbf{u}_j^1) \end{bmatrix},$$

$$\det[\Sigma_j^1(\mathbf{u}_j^1)] = \det(\Sigma_N^{j1}) \times \det[\mathbf{C}(\mathbf{u}_j^1)], \quad \text{where}$$

$$\mathbf{C}(\mathbf{u}_j^1) = \Sigma_F^{j1}(\mathbf{u}_j^1) + \Sigma_b^{j1} - \Sigma_{F,N}^{j1}(\mathbf{u}_j^1) \Sigma_N^{j1} \Sigma_{F,N}^{j1}(\mathbf{u}_j^1)^\top. \quad (17)$$

4.3 PC-level calibration results

Isolating each $\{K_d, k_c, C_d, c_c\}$, but leveraging strong linear correlation across frequencies ($4 \times 4 = 16$ total outputs), eliminates redundant information and brings the unit of analysis down fourfold to 4. The computational merits of OSSs, ported to a PC basis, enables efficient modular optimization and fully Bayes inference on parameter(s) \mathbf{u}_j^1 . Here we present the outcome of such analysis with an eye toward a fully combined setup in Section

5. We focus on contrasting to two earlier views, from a fully independent, separated (16-fold) analysis provided in Section 3.1.

Figure 3 shows 1d posterior marginals for \mathbf{u}_j^1 , for each $j = 1, \dots, 4$, alongside their 28Hz-only analog. With four coordinates of \mathbf{u} , a total of sixteen comparisons may be made with this view. Observe, for example, that u_1 , u_2 , and u_4 show considerable concentration of density under PC for outputs C_d and c_c . There is also a considerable shift in the location of posterior mass (i.e., the MAP), with u_1 and u_2 shifting up and u_4 shifting down for c_c . The rest of the PC marginals are similar to their 28Hz counterparts.

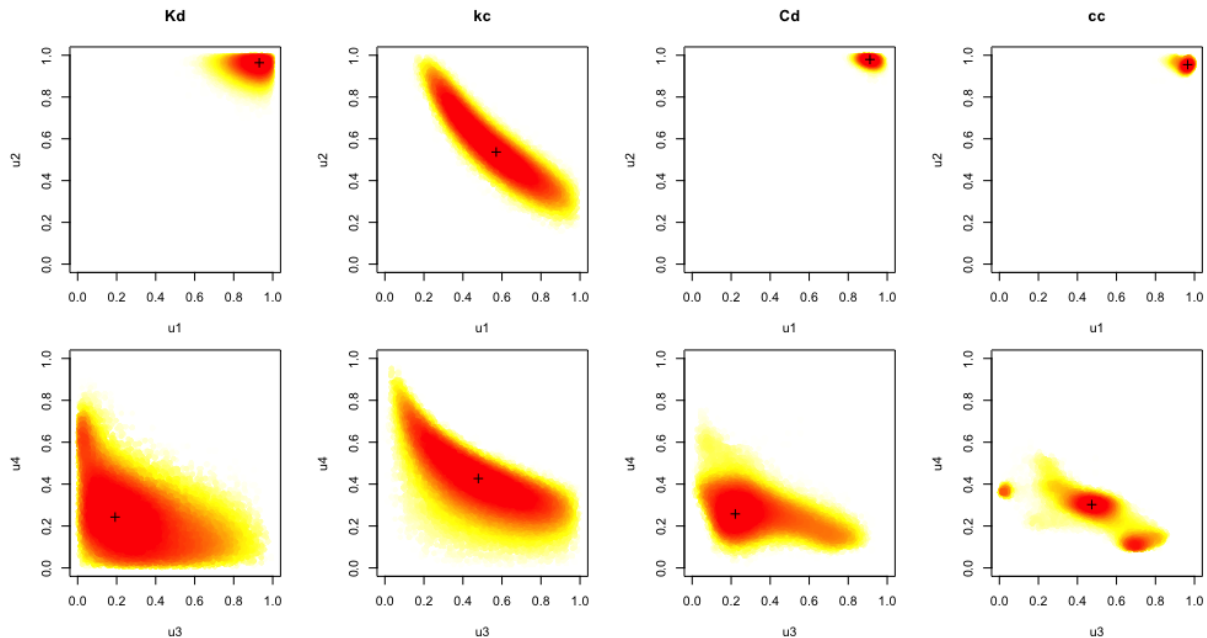


Figure 7: Bivariate marginal plots of posterior samples of \mathbf{u}_j^1 from PC-combined outputs K_d, k_c, C_d , and c_c . Dots are 100,000 MCMC samples of \mathbf{u}_j^1 , heat colored according to the rank of (log) posterior probability. The “+” indicates the MAP values.

Figure 7 offers a similar comparison in 2d when contrasted with Figure 4 in Section 3.1. As in that view, only a subset of pairs of outputs are shown. The rest are in Supplement A.2. Notice the marked improvement in posterior concentration in the rightmost four panels. Two of those panels, $(u_3 \times u_4)$ for C_d and (u_1, u_2) for c_c , also show substantial re-location of density compared to their 28Hz analog. The leftmost four panels offer less

stark contrast, a view shared by the 1d analysis in Figure 3.

These results indicate that we are headed in the right direction. We embarked on this analysis knowing well that the diversity of information across output frequencies would not be substantial. Nevertheless, representing it in a parsimonious way, through first-PCs, seems to enhance posterior concentration even though data is being discarded (i.e., the other three PCs). This is a hallmark of enhanced learning through dimension reduction. The last step is to combine these separate analyses into one, forming a posterior for a single set of unknowns given the entirety of data on all simulation and field outputs.

5 Full integration of outputs

The final step in our analysis is, in some sense, the easiest – that is, once all the hard work of building OSSs, forming first-PC posteriors, etc., is done. After detailing how outputs $j = 1, \dots, J$ may be combined, we provide a final suite of views into a unified posterior for \mathbf{u}^1 . Although the setup is rather generic in j , in what follows we continue to focus the discussion on the honeycomb application in anticipation of those results.

5.1 Inferential apparatus

Section 4.1 demonstrated that a PC basis is effective as a dimension reduction tool for four pairs of four honeycomb output frequencies. Those four separately calculated bases capture around a $4 \times 90\% \approx 360\%$ -fold larger amount of multivariate variability as compared to each single univariate output. On the other hand, each output property j (direct/cross stiffness or damping) has a distinct physical meaning. Dependence between them is highly non-linear, despite the linear form of the differential equation linking them (7). In Figure 5 we saw no evidence of strong linear dependence across the $J = 4$ output classes, which nudged us toward an independence assumption into this joint analysis. We shall return to that in our discussion in Section 7.

As a related but practical matter, each output is measured on a different scale. PCA helps here. Standardization of the 16d raw outputs, as a pre-processing step, followed by orthogonal projection onto the 4-column subspaces spanned by their first eigenvectors \mathbf{w}_j^1 , naturally place those quantities on an equal footing. Besides being represented in the direction of highest variability, they are scale-free which simplifies joint modeling downstream.

Modular calibration via optimization. Recall that each OSS, i.e., $F \times J \times K = 4,672$ univariate fits [Section 3.2] involves a manageable $\mathcal{O}(n_i^3)$ calculation. Then each of $K = 4$ output frequencies are combined into their first-PC (12). Finally, combine these representations together into a unified objective to obtain a single \mathbf{u}^1 under Eq. (4) for all ($J = 4$) observed discrepancies, with modular inference for GP hyperparameter ϕ_j^1 in each subspace. So basically we wish to jointly optimize multiple Eq. (4)’s for a single \mathbf{u}^1 via tuning \mathbf{u}_j^1 on observed discrepancies $\mathbf{D}_F^{j1}(\mathbf{u}_j^1) = (\mathbf{X}_F, (\mathbf{Y}_j^F - \hat{\mathbf{Y}}_j^M(\mathbf{u}_j^1))\mathbf{w}_j^1)$, for $j = 1, \dots, J$. After imposing conditional independence given common \mathbf{u}^1 , the following joint objective across all J outputs is immediate:

$$\hat{\mathbf{u}}^1 = \arg \max_{\mathbf{u}^1} \left\{ p(\mathbf{u}^1) \prod_{i=1}^J \left[\max_{\phi_j^1} p_b(\phi_j^1 \mid \mathbf{D}_F^{j1}(\mathbf{u}^1)) \right] \right\}. \quad (18)$$

In practice it easiest to solve this in log space. For each value of \mathbf{u}^1 entertained by a numerical optimizer, evaluation requires GP fitting for $J = 4$ observed discrepancies $\mathbf{D}_F^{j1}(\mathbf{u}_j^1)$, each with optimized GP hyperparameter $\hat{\phi}_j^1$ offloaded to a separate, library-facilitated, numerical optimizer. Each of J inner optimizations over hyperparameter ϕ_j^1 in $p_b(\phi_j^1 \mid \mathbf{D}_F^{j1}(\mathbf{u}^1))$ is wrapped in an outer optimization over the product-form joint marginal likelihood with prior $p(\mathbf{u}^1)$. To leverage ubiquitous modern multi-core workstation resources, we fit these in parallel. Following Huang et al. (2020), we use `optim` with BFGS in R for the inner GP hyperparameter optimization(s) and `nloptr` wrapped in a multi-start scheme for the outer optimization to find $\hat{\mathbf{u}}^1$.

Bayesian joint inference. Posterior sampling \mathbf{u}^1 may follow similar principles. Conditioning on the optimized hyperparameters $\hat{\phi}_j^1$, with the j^{th} output in first-PC representation, i.e., \mathbf{y}_j^{F1} and \mathbf{y}_j^{M1} via Eq. (12), a joint posterior via conditional independence follows from a likelihood in product form:

$$p(\mathbf{u}^1 \mid \mathbf{y}_1^{F1}, \mathbf{y}_1^{M1}, \dots, \mathbf{y}_J^{F1}, \mathbf{y}_J^{M1}) \propto p(\mathbf{u}^1) \cdot \prod_{j=1}^J p(\mathbf{y}_j^{F1}, \mathbf{y}_j^{M1} \mid \mathbf{u}^1). \quad (19)$$

To sample from this posterior, a Metropolis-within-Gibbs scheme can be easily coded up, with each Gibbs step taking a marginal Gaussian random walk on \mathbf{u}^1 . Under the multivariate OSSs emulation structure, Metropolis rejection for \mathbf{u}^1 can be broken down to evaluation of each (log) MVN-likelihood, $p(\mathbf{y}_j^{F1}, \mathbf{y}_j^{M1} \mid \mathbf{u}^1)$, for $j = 1, \dots, J$. We see potential for each to be evaluated in parallel and then put together into the joint (log) likelihood. Still, our serial implementation (with vectored linear algebra subroutines) was fast enough to furnish thousands of samples/hour. A modular optimization solution (18) was helpful in providing a warm-start to minimize burn-in efforts.

5.2 Joint results

Here we present views into our fully integrated calibration results. Our modular optimization(s) utilized a 500-random-multi-start BFGS implemented in parallel. Although more time is required for jointly optimizing four separate sub-objectives at each iteration, the overall waiting time for joint optimization turns out to be comparable to univariate and PC-based variations. A post-optimization analysis summarizes the median number of `nloptr` iterations until convergence for each methods from 500 random initialization: 335 for PC- K_d , 114 for PC- k_c , 552 for PC- C_d , 430 for PC- c_c , and 117 for the unified approach. Speed of the unified approach may owe to the flatter/smooth surface, shown momentarily. For full Bayes via MCMC, the running time is also comparable to its univariate and PC counterparts, thanks to the multiple, and highly parallelizable, and sparse OSS covariance.

Figure 8 provides a 2d look via full posterior (bottom-left triangle) and multi-start optimization (top-right) and univariate marginals (diagonal). This may be contrasted with any of the PC-level analogues in Supplement A.2 to reveal how information is synthesized across outputs in this joint analysis. While the optimized solutions demonstrate how

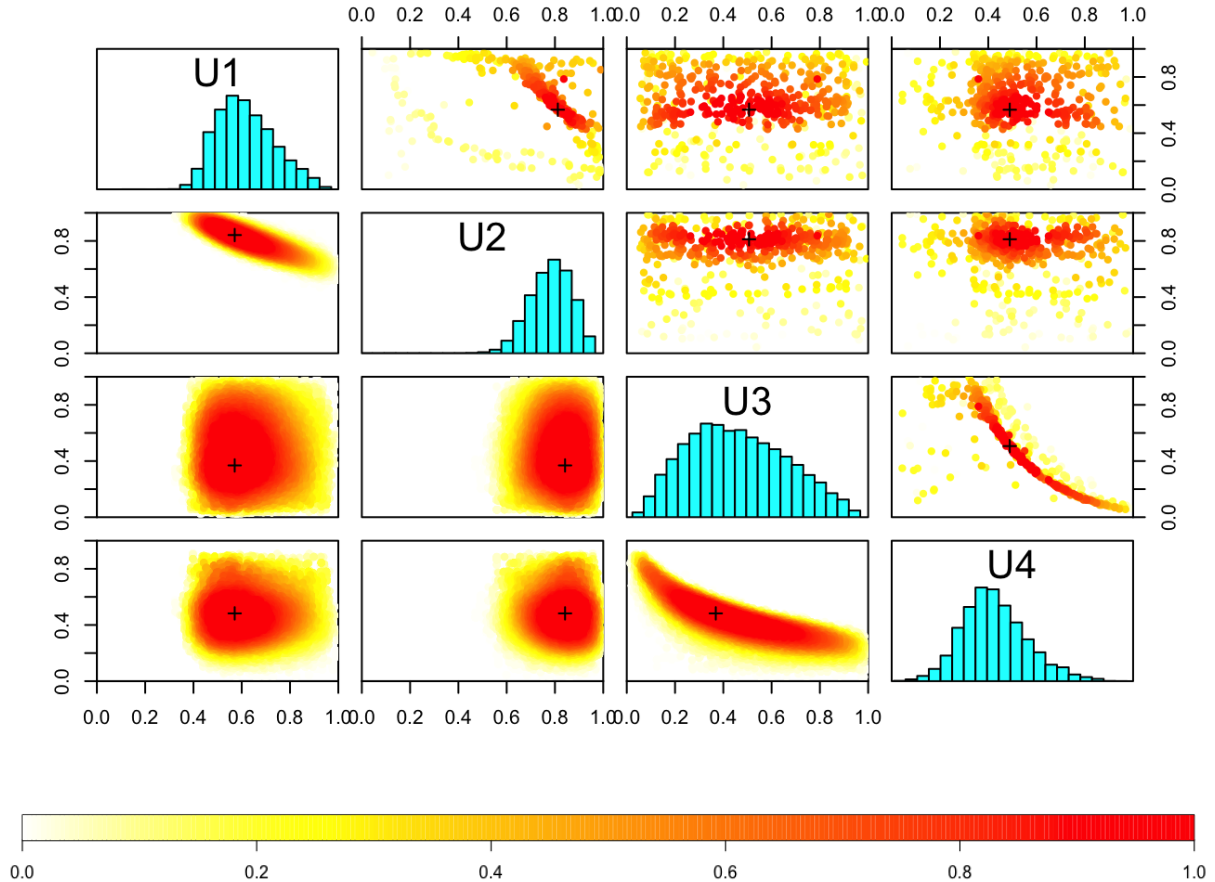


Figure 8: Fully Bayesian (lower and diagonal) and modular optimization (upper) calibration results for \mathbf{u}^1 from the unified approach combining all 16 outputs. Heat color are derived from rank of (joint) log posterior probability of these parameter values. Bayesian results are from 100,000 MCMC samples after burn-in. Optimization results are from 500 converged optimization under random initialization. “+” signs indicate the MAP values.

local dynamics challenge optimization, its MAP estimation and high density regions are comparable to the fully Bayesian ones. From both approaches, two dependent structures between pairs of parameter (u_1, u_2) and (u_3, u_4) can be observed, displaying an interesting relationship between the friction coefficients (u_1, u_2) and friction exponents (u_3, u_4) .

Our BHGE colleagues concluded that this pattern may be explained by an underlying turbulent-lubrication friction factor model from bulk-flow theory (Hirs, 1973).

Figure 9 is lower resolution, providing a 1d look, but allows a more visually immediate comparison. Here we see how each output property contributes to the final global solution

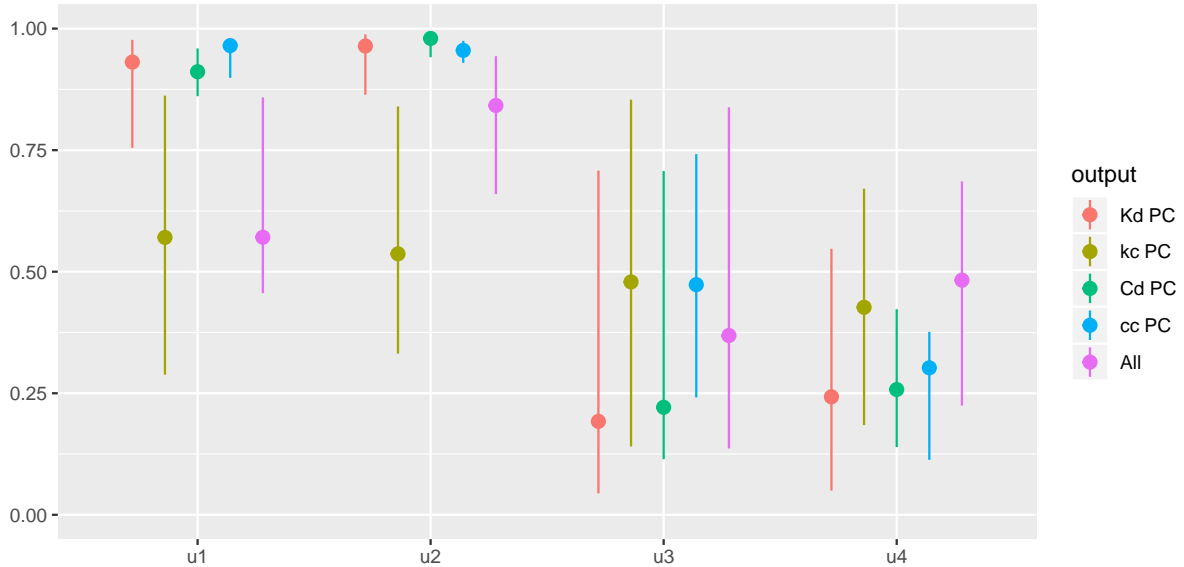


Figure 9: Side-by-side comparison between marginal posterior distributions of $\mathbf{u}_j^1, j = 1, \dots, 4$ from outputs $K_d, k_c, C_d,$ and c_c (labeled “PC”) and \mathbf{u}^1 via unified output (labeled “All”). Dots indicate MAP values and error bars form 90% credible intervals.

\mathbf{u}^1 , with the output property. Apparently, cross stiffness (k_c) is the most influential. Notice the similarity between the \mathbf{u}^1 posterior distribution with k_c PC posterior \mathbf{u}_2^1 in each of the u dimensions, especially in u_1 . Further comparisons in 2d, via both the \mathbf{u}^1 marginals in Figure 8 and PC-calibrated \mathbf{u}_2^1 marginals shown in Figure 15 from Supplement A.2, demonstrate dependence in parameters (u_1, u_2) .

When comparing the landscape of solutions in upper triangle of Figure 8 with those from Figures 15–16 one immediately appreciates the benefit of a smoother posterior surface via full integration. Notice in those figures that the optimized solutions from outputs K_d, C_d and c_c are quite concentrated in very small (dense red) peaks, in contrast to the much flatter surfaces from k_c [Figure 15] and the fully integrated [Figure 8]. The full Bayes (lower and diagonal) marginals further exhibit this pattern: fully integrated and PC- c_c

exhibit flatter posteriors, with two ridges in (u_1, u_2) and (u_3, u_4) ; the other three PC-based results produce much narrower peaked posterior surfaces, specially in dimension of (u_1, u_2) . Interestingly, different outputs could contribute unequally to the fully integrated result [Figure 8], possibly due to different amount of signal versus noise for the output relative to the rest. In the fully integrated honeycomb analysis, output k_c seems to pull the parameter posterior towards itself more than the other three outputs, especially in the (u_1, u_2) subspace (See Figure 9).

To explore sensitivity to priors and forms of discrepancy, Supplement A.4 demonstrates how these posteriors vary, but are ultimately quite robust to prior misspecification. This extends Huang et al.’s limited, but ultimately similar analysis in the single-output setting. For example, uniform rather than Beta(2, 2) priors on \mathbf{u}^1 results heavier concentration of posterior mass near the boundaries of the study region. Weak “prescient” (greater prior concentration on the posterior MAP), and “weak” adversarial (prior concentration away from the MAP) priors have little effect. Using L2 discrepancy, i.e., no GP on the bias, has rather more, and deleterious effect on prediction as we show next.

6 Prediction

Inference for the calibration parameter is often the primary interest in a KOH-style calibration exercise. Integrating over the posterior predictive distribution, say at $\mathbf{x}_{(\text{new})}$, alongside \mathbf{u} involves many of the same steps as above, except now with a MVN conditional distribution that has three components: field observed, simulated, and field unobserved (at $\mathbf{x}_{(\text{new})}$). In the univariate case and with ordinary, non-OSS surrogates, this is described in textbooks (e.g., Gramacy, 2020, Chapter 8.1.5). With OSSs for univariate output, Huang et al. (2020) demonstrate how the same conditioning is computationally tractable even for larger N by extending the block diagonal structure to the three-component predictive setup. An updated variation on those equations are provided here as Eq. (21) momentarily,

extending that setup to the multi-output setting. This is accompanied by predictive results and comparisons for the honeycomb, beginning in the basis space of the first-PC (i.e., via \mathbf{u}^1), and then back in original output spaces.

6.1 In-basis

Consider first-PC field outputs $\hat{\mathbf{y}}_j^{M1}(\mathbf{x}_{(\text{new})}, \cdot) + \hat{\mathbf{b}}_j^1(\mathbf{x}_{(\text{new})})$ for each of $j = 1, \dots, J$, where $J = 4$ for the honeycomb. This involves a direct, four-fold independent application of Huang et al. (2020). No new methodology is being developed here, however we find this a useful warm-up, thinking ahead to the building blocks required for a full multi-output setting next in Section 6.2 via Eq. (19). It also enlightening to compare these predictions to the simulation-only ones $\hat{\mathbf{y}}_j^{M1}(\mathbf{x}_{(\text{new})}, \cdot)$ as a lens into the nature of the bias $\hat{\mathbf{b}}_j^1(\mathbf{x}_{(\text{new})})$.

For example, Figure 10 shows leave-one-out cross-validated (LOO-CV) predictions for field outputs, $\hat{\mathbf{y}}_j^{F1}(\mathbf{X}_F)$, for K_d and k_c ($j = \{1, 2\}$), pitting prediction without bias correction $\hat{\mathbf{y}}_j^{M1}(\mathbf{X}_F, \hat{\mathbf{u}}^1)$ against bias corrected $\hat{\mathbf{y}}_j^{M1}(\mathbf{X}_F, \hat{\mathbf{u}}^1) + \hat{\mathbf{b}}_j^1(\mathbf{X}_F)$. Here, $\hat{\mathbf{u}}^1$ comes via samples from fully integrated posterior (19). Similar views for the other two outputs may be found in Figure 17 of Supplement A.3. Observe in both cases that predictions with-

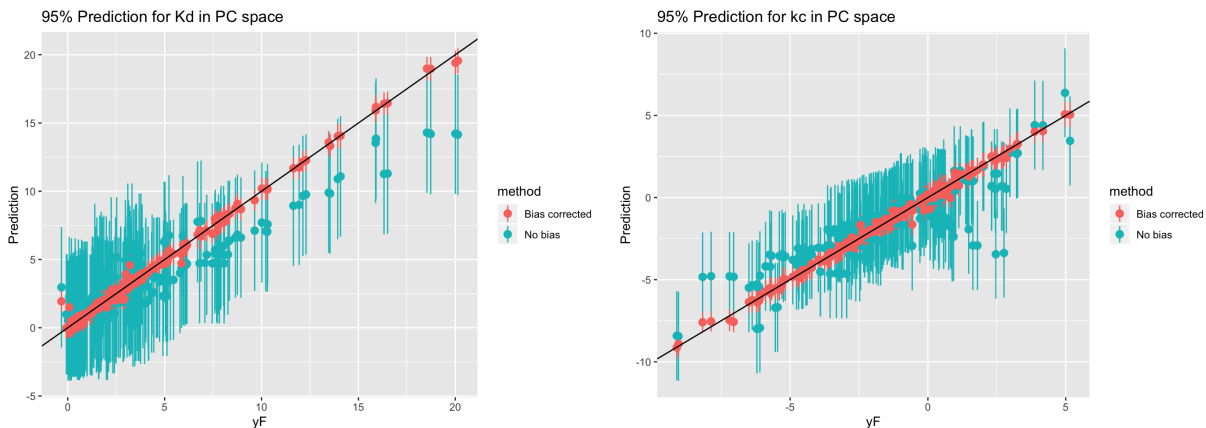


Figure 10: LOO-CV first-PC posterior predictive summaries for direct stiffness K_d and cross stiffness k_c . Intervals trace out 95%; black line has intercept zero, slope one.

out bias correction (blue) exhibit noticeable deviation from the calibration (diagonal) line

with relatively large credible intervals, suggesting that a considerable portion of dynamics in the field are not fully captured by simulation. Bias correction (red) is essential, not only for accuracy but also for confidence: both have appropriate coverage, but one has much smaller intervals. Yet these two outputs also exemplify a dual role played by the bias correction term $\hat{\mathbf{b}}_j^1(\mathbf{X}_F)$. For K_d (left), discrepancies generally widen as the observed output K_d increases. For k_c (right), the observed model discrepancy demonstrates a more complicated pattern, with relatively larger discrepancies at the two extremes.

6.2 Original outputs

Poster predictive sampling of the original $J \times K$ outputs involves re-centering, re-scaling, and back-rotation from all the PC bases. Once \mathbf{u}^1 values are sampled from Eq. (19), we can feed these posteriors into multiple $J \times K$ OSSs $\hat{\mathbf{y}}_j^{Mk}(\mathbf{x}, \mathbf{u}^1)$ with their own bias corrections:

$$\mathbf{y}_j^{Fk}(\mathbf{x}) = \mathbf{y}_j^{Mk}(\mathbf{x}, \mathbf{u}^1) + \mathbf{b}_j^k(\mathbf{x}) + \epsilon_j^k, \quad j = 1, \dots, J, k = 1, \dots, K. \quad (20)$$

Fitted discrepancies $\hat{\mathbf{b}}_j^k(\mathbf{x})$ are required to recover the complete multiple-output prediction on original outputs, while only the lower-dimensional first-PC representations are needed for parameter learning and sampling at the PC (14) and fully integrated levels (19).

For the j^{th} output property, raw predictions at new site location $\mathbf{x}_{(\text{new})}$ are made by separately applying the OSSs kriging equations from Huang et al. (2020) $K = 4$ times, but now in their PC represented spaces, where their raw predictive mean and variances

$(\mu_{j(\text{new})}^k, \Sigma_{j(\text{new})}^k)$ in the basis spaces are still analytically tractable,

$$\begin{aligned}
\mu_{j(\text{new})}^k &= \Sigma_{F',F}^{jk} \mathbf{C}^{-1}(\mathbf{u}^1) [\mathbf{y}_j^{Fk} - \Sigma_{F,N}^{jk}(\mathbf{u}^1) (\Sigma_N^{jk})^{-1} \mathbf{y}_j^{Mk}] \\
&\quad + \Sigma_{F,N}^{jk(\text{new})}(\mathbf{u}^1) (\Sigma_N^{jk(\text{new})})^{-1} \mathbf{y}_j^{Mk}, \\
\Sigma_{j(\text{new})}^k &= \Sigma_{F'}^{jk(\text{new})}(\mathbf{u}^1) + \Sigma_b^{jk(\text{new})} - \Sigma_{F',F}^{jk} \mathbf{C}^{-1}(\mathbf{u}^1) (\Sigma_{F',F}^{jk})^\top \\
&\quad - \Sigma_{F',N'}^{jk(\text{new})}(\mathbf{u}^1) (\Sigma_{N'}^{jk(\text{new})})^{-1} [\Sigma_{F',N'}^{jk(\text{new})}(\mathbf{u}^1)]^\top.
\end{aligned} \tag{21}$$

Details on each new notational element are provided in Supplement A.3.

Seeking insights in an out-of-sample setting, we performed LOO-CV for the honeycomb like in Section 6.1, but this time in the original output space. Using Eq. (21) we first obtain the full-rank raw predictions in the PC spaces,

$$(\mathbf{y}_j^{Fk} \mid \mathbf{y}_{-i}^{Mk}, \mathbf{y}_{-i}^{Fk}, \mathbf{y}_i^{Mk}, \Phi, \mathbf{u}^1) \sim \mathcal{N}_i(\mu_{ji}^k, \Sigma_{ji}^k), \quad i = 1, \dots, F, \quad j = 1, \dots, J, \quad k = 1, \dots, K.$$

Once K raw predictions for the j^{th} output property $\mathbf{Y}_j^{FK} = (\mathbf{y}_j^{F1}, \dots, \mathbf{y}_j^{Fk}, \dots, \mathbf{y}_j^{FK})$ in basis spaces are sampled, they may be rotated back at once using the full matrix \mathbf{W}_j of the centered and scaled eigenvectors through $\mathbf{W}_j^{-1} \mathbf{Y}_j^{FK} = \mathbf{Y}_j^F, j = 1, \dots, J$, all at once. After this fashion, predictions thus obtained synthesize more information than a univariate analysis could. Since a common \mathbf{u}^1 sample is used for all k , predictive uncertainty may be dramatically reduced. We take ten thousand MCMC posterior samples \mathbf{u}^1 and calculate predictive moments using the laws of total expectation and variance:

$$\mathbb{E}(\mathbf{y}_j^{Fk} \mid \cdot) = \mathbb{E}[\mathbb{E}(\mathbf{y}_j^{Fk} \mid \cdot, \mathbf{u}^1)], \quad \text{and} \quad \mathbb{V}(\mathbf{y}_{(\text{new})}^F \mid \cdot) = \mathbb{V}[\mathbb{E}(\mathbf{y}_j^{Fk} \mid \cdot, \mathbf{u}^1)] + \mathbb{E}[\mathbb{V}(\mathbf{y}_j^{Fk} \mid \cdot, \mathbf{u}^1)].$$

These quantities then approximate the full posterior (out-of-sample) predictive distribution at any $\mathbf{x}_{(\text{new})}$: $(\mathbf{y}_j^{Fk} \mid \mathbf{y}_{-i}^{Mk}, \mathbf{y}_{-i}^{Fk}, \mathbf{y}_i^{Mk}, \Phi), \forall i, j, k$.

Table 1 summarizes the 16 LOO-CV RMSEs recovered back in the original $J = 4$ output

properties at $K = 4$ frequencies. For example, these fully Bayesian LOO-CV predictions for direct stiffness K_d at 28 Hz across $F = 292$ sites have RMSE of 1.460. This bests its univariate, separately calibrated counterpart in Huang et al. (Table 1) with RMSE of 1.957. Although not surprising, we speculate this is likely due to better parameter identification and discrepancy learning through synthesis of a larger corpus of training data. For another

Output	28 Hz	70 Hz	126 Hz	154 Hz
K_d	1.460	1.407	1.313	1.442
k_c	0.869	0.901	0.880	1.120
C_d	2.994	3.049	2.742	2.762
c_c	3.867	2.492	2.028	1.535

Table 1: LOO-CV RMSEs using multiple-output approach. Rounded at 3 digits.

view of LOO-CV performance in original outputs, we plotted posterior predictive mean and 95% intervals over each observed field output. Figure 11 provides these for direct stiffness K_d with $K = 4$ frequencies; results for the other three outputs are provided by Figures 18–20 in Supplement A.3. Comparing K_d at 28 Hz to its univariate counterpart in Figure 11 of Huang et al. (2020), this multiple-output approach yields more closely aligned out-of-sample predictions, with fewer and less substantial deviations from the diagonal (black) line. Moreover, there are no obvious sites with larger level of predictive uncertainty (wider error-bars). Notice in Figure 11 that there are only a few sites which are mis-predicted and that the error bars are more uniform than those in Huang et al. version. Across frequency, predictive uncertainty (error-bar width) decreases as the frequency level increases. The first three outputs K_d , k_c , and C_d exhibit stable predictive performance. The last output, c_c , reflects high measurement error. Refer Figure 20 to Figure 17.

7 Discussion

Motivated by a large-scale industrial multivariate calibration problem studding (honeycomb) seal flow dynamics from oil and gas research, we developed a new multivariate cal-

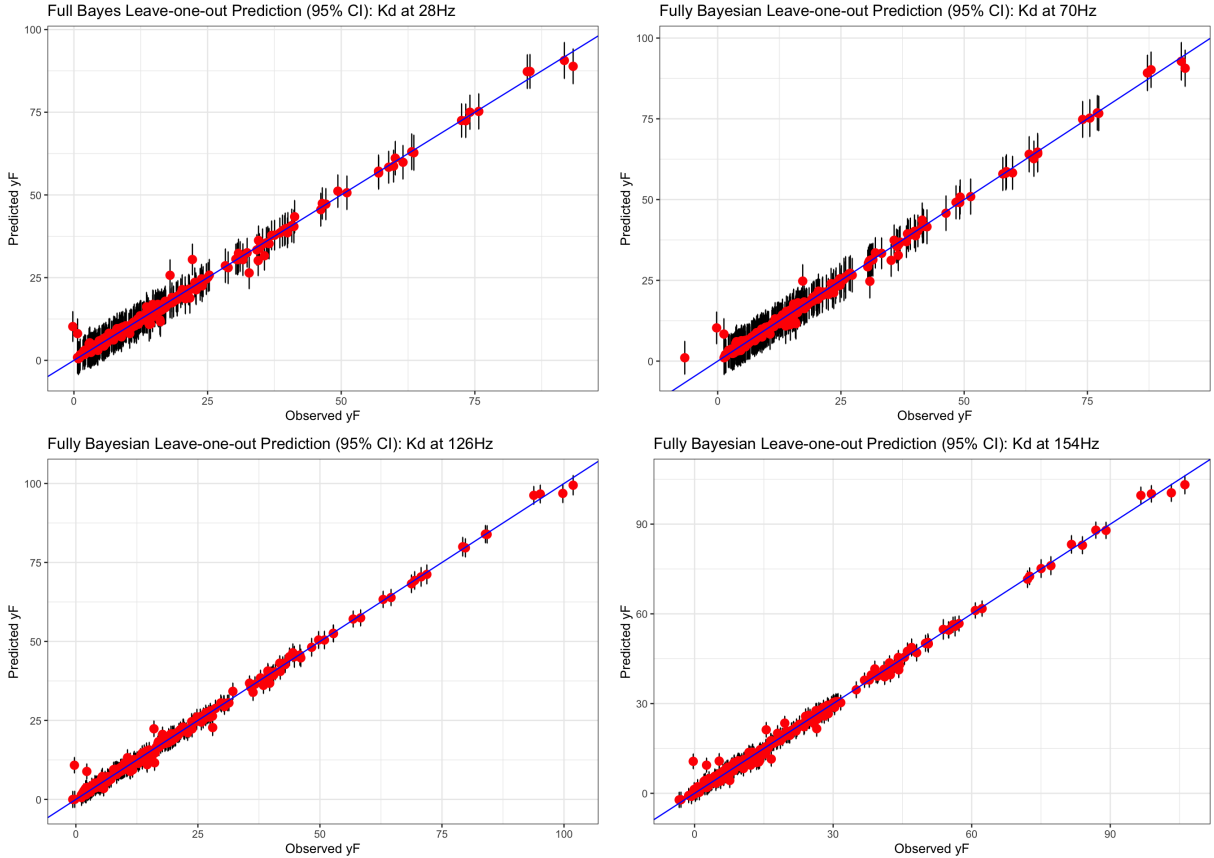


Figure 11: Posterior predictive comparison for direct stiffness K_d at 28, 70, 126, and 154 Hz. Red dots are the predicted mean and black bars are 95 % credible intervals.

ibration method by extending a few features of a parsimonious univariate strategy based on on-site surrogates (OSSs; Huang et al., 2020). Tailored to effectively capture unique simulation features including high-dimensional input space, local nonstationary, missing simulations, and model fidelity at scale, this method is practical, but it is not without drawbacks. Univariate output applications, when replicated across diverse outputs are not immune to a data-poor Bayesian learning pitfalls for both high-dimensional calibration parameter and ill-posed model discrepancy. Therefore, in lieu of imposing elaborate cross-site correlation structures, we opted for a simpler approach.

Our solution, toward a multivariate OSS-based calibration, gathered together responses to several features of the honeycomb. Although this multivariate setup might not be ideal for all applications, especially when the ground truth posterior distribution of parame-

ter \mathbf{u} differ strikingly across different outputs, see e.g., Box and Draper (1965), the focus here is to leverage all available information through one coherent, and tractable modeling framework. A careful exploratory data analysis (EDA) suggested that a principal component-style basis representation could be effective for handling honeycombs quadruplet of highly linearly dependent output frequencies. We then update the OSS framework for both modular/optimized and fully Bayesian implementations PC-based calibration within the Kennedy & O’Hagan framework. Our empirical results indicated improved parameter identification and posterior concentration for calibration parameters, compared to the (separate) univariate analog. Then, we designed an independent multi-output PC approach to gather these models across output property. This was motivated by a lack of linear correlation observed in our EDA. The result is a unified analysis for the honeycomb, synthesizing millions of simulation runs in a matter of hours.

It might be possible to entertain nonlinear dependency among output properties, as suggested by the differential equation (7) known to govern relationships across outputs of the types studied in honeycomb. On the other hand though, our visual inspections (via EDA) did not reveal any notable patterns. So at this time, the merits of such an approach are speculative at best, although extension is certainly possible. Given posterior draws of the calibration parameter, analytically tractable prediction is within reach. We evaluated empirical out-of-sample performance in PC-basis spaces and back on original outputs. This analysis reinforces the existence of nontrivial model discrepancies for all outputs as well as the integral role of KOH bias correction. Compared to its univariate, separately calibrated counterpart, this unified multiple-output solution enjoys improved out-of-sample accuracy.

Supplementary Material

Supplementary Material: The PDF file contains (A.1) univariate calibration results: full Bayes for 16 outputs; (A.2) PC-level calibration results: optimization and full Bayes; (A.3) Multiple-output OSSs prediction results; and (A.4) Sensitivity analysis.

Computer Code: R code to reproduce all the results in this article are available on a private repository on Bitbucket, available from the authors (many aspects are proprietary to BHGE and require approval). Note that execution requires thousands of core hours even in high performance computing environments.

Acknowledgments

Authors JH and RBG are grateful for support from National Science Foundation grants DMS-1521702 and DMS-1821258. JH and RBG also gratefully acknowledge funding from a DOE LAB 17-1697 via subaward from Argonne National Laboratory for SciDAC/DOE Office of Science ASCR and High Energy Physics. We thank Andrea Panizza (BHGE) for early work on this project, and for initiating the line of research, Mirko Libraschi (BHGE) for many interesting discussions, and thoughtful comments from the Editor V. Roshan Joseph, an AE, and two referees towards improving this work.

References

- Arendt, P. D., Apley, D. W., Chen, W., Lamb, D., and Gorsich, D. (2012). “Improving identifiability in model calibration using multiple responses.” *Journal of Mechanical Design*, 134, 10, 100909.
- Bayarri, M., Berger, J., Garcia-Donato, G., Liu, F., Paulo, R., Sacks, J., Palomo, J.,

- Walsh, D., Cafeo, J., and Parthasarathy, R. (2007). “Computer Model Validation with Functional Output.” *Annals of Statistics*, 35, 5, 1874–1900.
- Bayarri, M. J., Berger, J. O., Calder, E. S., Dalbey, K., Lunagomez, S., Patra, A. K., Pitman, E. B., Spiller, E. T., and Wolpert, R. L. (2009). “Using statistical and computer models to quantify volcanic hazards.” *Technometrics*, 51, 4, 402–413.
- Box, G. E. P. and Draper, N. R. (1965). “The Bayesian Estimation of Common Parameters from Several Responses.” *Biometrika*, 52, 3 & 4, 355–365.
- Brynjarsdóttir, J. and O’Hagan, A. (2014). “Learning about physical parameters: The importance of model discrepancy.” *Inverse Problems*, 30, 11, 114007.
- Childs, D. (1993). *Turbomachinery Rotordynamics: Phenomena, Modeling, and Analysis*. New York, NY: John Wiley & Sons, Inc.
- Conti, S. and O’Hagan, A. (2010). “Bayesian emulation of complex multi-output and dynamic computer models.” *Journal of statistical planning and inference*, 140, 3, 640–651.
- Delgado, A., Librashi, M., and Vannini, G. (2012). “Dynamic Characterization of Tilting Pad Journal Bearings From Component and System Level Testing.” *ASME Turbo Expo 2012: Turbine Technical Conference and Exposition*. DOI: 10.1115/GT2012-69851.
- D’Souza, R. J. and Childs, D. W. (2002). “A Comparison of Rotordynamic-Coefficient Predictions for Annular Honeycomb Gas Seals Using Three Different Friction-Factor Models.” *Journal of Tribology*, 124, 3, 524–529.
- Fadikar, A., Higdon, D., Chen, J., Lewis, B., Venkatramanan, S., and Marathe, M. (2018). “Calibrating a Stochastic Agent Based Model Using Quantile-based Emulation.” *SIAM/ASA Journal on Uncertainty Quantification*, 6, 4, 1685–1706.

- Gramacy, R. B. (2020). *Surrogates: Gaussian Process Modeling, Design and Optimization for the Applied Sciences*. Boca Raton, Florida: Chapman Hall/CRC. <http://bobby.gramacy.com/surrogates/>.
- Gramacy, R. B. and Apley, D. W. (2015). “Local Gaussian process approximation for large computer experiments.” *Journal of Computational and Graphical Statistics*, 24, 2, 561–578.
- Gramacy, R. B., Bingham, D., Holloway, J. P., Grosskopf, M. J., Kuranz, C. C., Rutter, E., Trantham, M., and Drake, R. P. (2015). “Calibrating a large computer experiment simulating radiative shock hydrodynamics.” *Annals of Applied Statistics*, 9, 3, 1141–1168.
- Gu, M. (2019). “Jointly robust prior for Gaussian stochastic process in emulation, calibration and variable selection.” *Bayesian Analysis*, 14, 3, 857–885.
- Gu, M. and Berger, J. O. (2016). “Parallel partial Gaussian process emulation for computer models with massive output.” *Annals of Applied Statistics*, 10, 3, 1317–1347.
- Gu, M. and Wang, L. (2018). “Scaled Gaussian Stochastic Process for Computer Model Calibration and Prediction.” *SIAM/ASA Journal on Uncertainty Quantification*, 6, 4, 1555–1583.
- Guinness, J. (2019). “Spectral density estimation for random fields via periodic embeddings.” *Biometrika*, 106, 2, 267–286.
- Higdon, D., Gattiker, J., Williams, B., and Rightley, M. (2008). “Computer model calibration using high-dimensional output.” *Journal of the American Statistical Association*, 103, 482, 570–583.
- Higdon, D., Kennedy, M., Cavendish, J. C., Cafo, J. A., and Ryne, R. D. (2004). “Combining

- ing field data and computer simulations for calibration and prediction.” *SIAM Journal on Scientific Computing*, 26, 2, 448–466.
- Hirs, G. G. (1973). “A Bulk-Flow Theory for Turbulence in Lubricant Films.” *Journal of Lubrication Technology*, 95, 2, 137–145.
- Huang, J., Gramacy, R. B., Binois, M., and Libraschi, M. (2020). “On-site surrogates for large-scale calibration.” *Applied Stochastic Models in Business and Industry*, 36, 2, 283–304. Preprint on arXiv:1810.01903.
- Jiang, Z., Arendt, P., Apley, D., and Chen, W. (2016). “Multi-response Approach to Improving Identifiability in Model Calibration.” In *Handbook of Uncertainty Quantification*. New York: Springer.
- Johnson, L. (2008). “Microcolony and Biofilm Formation as a Survival Strategy for Bacteria.” *Journal of Theoretical Biology*, 251, 24–34.
- Kennedy, M. C. and O’Hagan, A. (2001). “Bayesian calibration of computer models (with discussion).” *Journal of the Royal Statistical Society, Series B*, 63, 3, 425–464.
- Kita, H., Taniguchi, K., and Nakajima, Y. (2016). *Realistic Simulation of Financial Markets: Analyzing Market Behaviors by the Third Mode of Science*, vol. 4. Springer.
- Kleynhans, G. and Childs, D. (1997). “The Acoustic Influence of Cell Depth on the Rotordynamic Characteristics of Smooth-Rotor/Honeycomb-Stator Annular Gas Seals.” *ASME Journal of Engineering for Gas Turbines and Power*, 949–957.
- Liu, F., Bayarri, M., and Berger, J. (2009). “Modularization in Bayesian analysis, with emphasis on analysis of computer models.” *Bayesian Analysis*, 4, 1, 119–150.
- Marcy, P. W. and Storlie, C. B. (2020). “Bayesian Calibration of Computer Models with Informative Failures.” Preprint on arXiv:2006.07546.

- Marmin, S. and Filippone, M. (2022). “Deep Gaussian Processes for Calibration of Computer Models.” *Bayesian Analysis*, 1, 1, 1–30.
- McFarland, J., Mahadevan, S., Romero, V., and Swiler, L. (2008). “Calibration and uncertainty analysis for computer simulations with multivariate output.” *AIAA journal*, 46, 5, 1253–1265.
- Mehta, P., Walker, A., Lawrence, E., Linares, R., Higdon, D., and Koller, J. (2014). “Modeling satellite drag coefficients with response surfaces.” *Advances in Space Research*, 54, 8, 1590–1607.
- Morris, M. D. and Mitchell, T. J. (1995). “Exploratory designs for computational experiments.” *Journal of Statistical Planning and Inference*, 43, 381–402.
- Paulo, R., Garcia-Donato, G., and Palomo, J. (2012). “Calibration of computer models with multivariate output.” *Computational Statistics and Data Analysis*, 56, 12, 3959–3974.
- Petersen, K. B. and Pedersen, M. S. (2008). “The matrix cookbook.” *Technical University of Denmark*, 7, 15.
- Plumlee, M. (2017). “Bayesian calibration of inexact computer models.” *Journal of the American Statistical Association*, 112, 519, 1274–1285.
- (2019). “Computer model calibration with confidence and consistency.” *Journal of the Royal Statistical Society: Series B*, 81, 3, 519–545.
- Santner, T. J., Williams, B. J., and Notz, W. I. (2018). *The design and analysis of computer experiments, 2nd Edition*. Springer Science & Business Media.
- Tuo, R. and Wu, C. F. J. (2015). “Efficient calibration for imperfect computer models.” *Annals of Statistics*, 43, 6, 2331–2352.

— (2016). “A Theoretical Framework for Calibration in Computer Models: Parameterization, Estimation and Convergence Properties.” *Journal of Uncertainty Quantification*, 4, 767–795.

Wong, R. K. W., Storlie, C. B., and Lee, T. C. M. (2017). “A Frequentist Approach to Computer Model Calibration.” *Journal of the Royal Statistical Society: Series B (Statistical Methodology)*, 79, 2, 635–648.

Zhang, Y., Zhao, H., Hassinger, I., Brinson, L. C., Schadler, L. S., and Chen, W. (2015). “Microstructure reconstruction and structural equation modeling for computational design of nanodielectrics.” *Integrating Materials and Manufacturing Innovation*, 4, 1, 14.

A Supplementary Material

... for “Multi-output calibration of a honeycomb seal via on-site surrogates” by Huang and Gramacy.

A.1 Univariate calibration results: full Bayes for 16 outputs

We provide completed univariate \mathbf{u} posterior summaries for all 16 outputs: K_d , k_c , C_d , and c_c , each at 28, 70, 126, and 154 Hz, augmenting Figure 12’s marginal view. Observe greater differences between output properties (block), than across frequencies (color). Augmenting

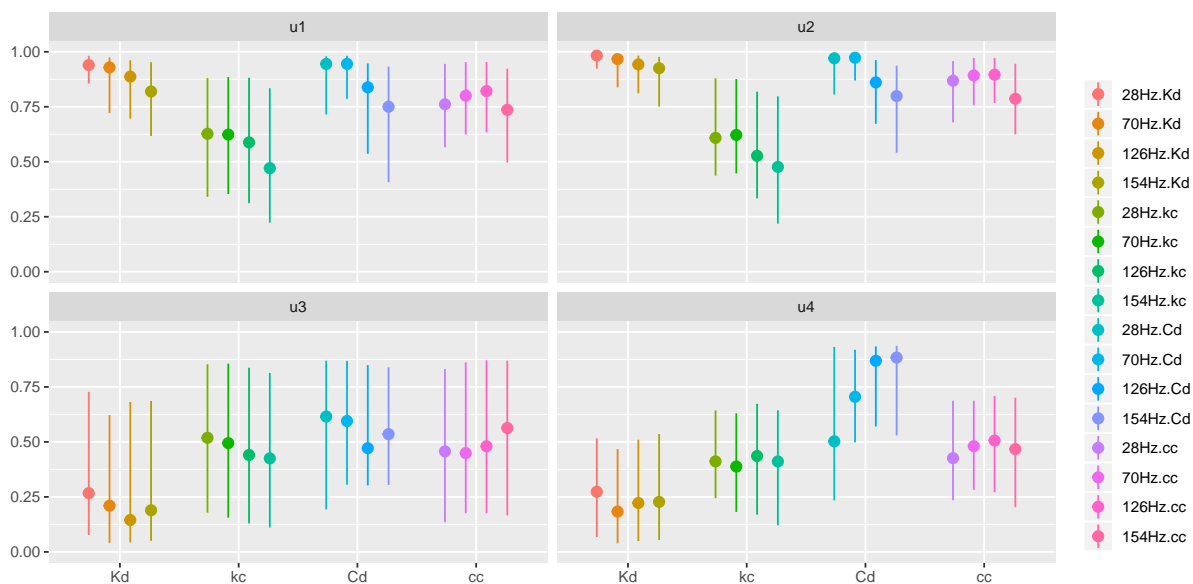


Figure 12: 16 sets of marginal \mathbf{u} posteriors from outputs K_d , k_c , C_d , and c_c at frequencies 28, 70, 126, and 154 Hz. Dots indicate MAP values and error bars form 90% intervals.

those 1d marginals, Figures 13 and 14 project \mathbf{u} onto its six 2d marginals, separately for each frequency. Each row represents a complete set of 2d projections for one output property–frequency pair. Cross frequency consistency in MAP estimation and high density region can be observed from these figures, echoing Figure 12.

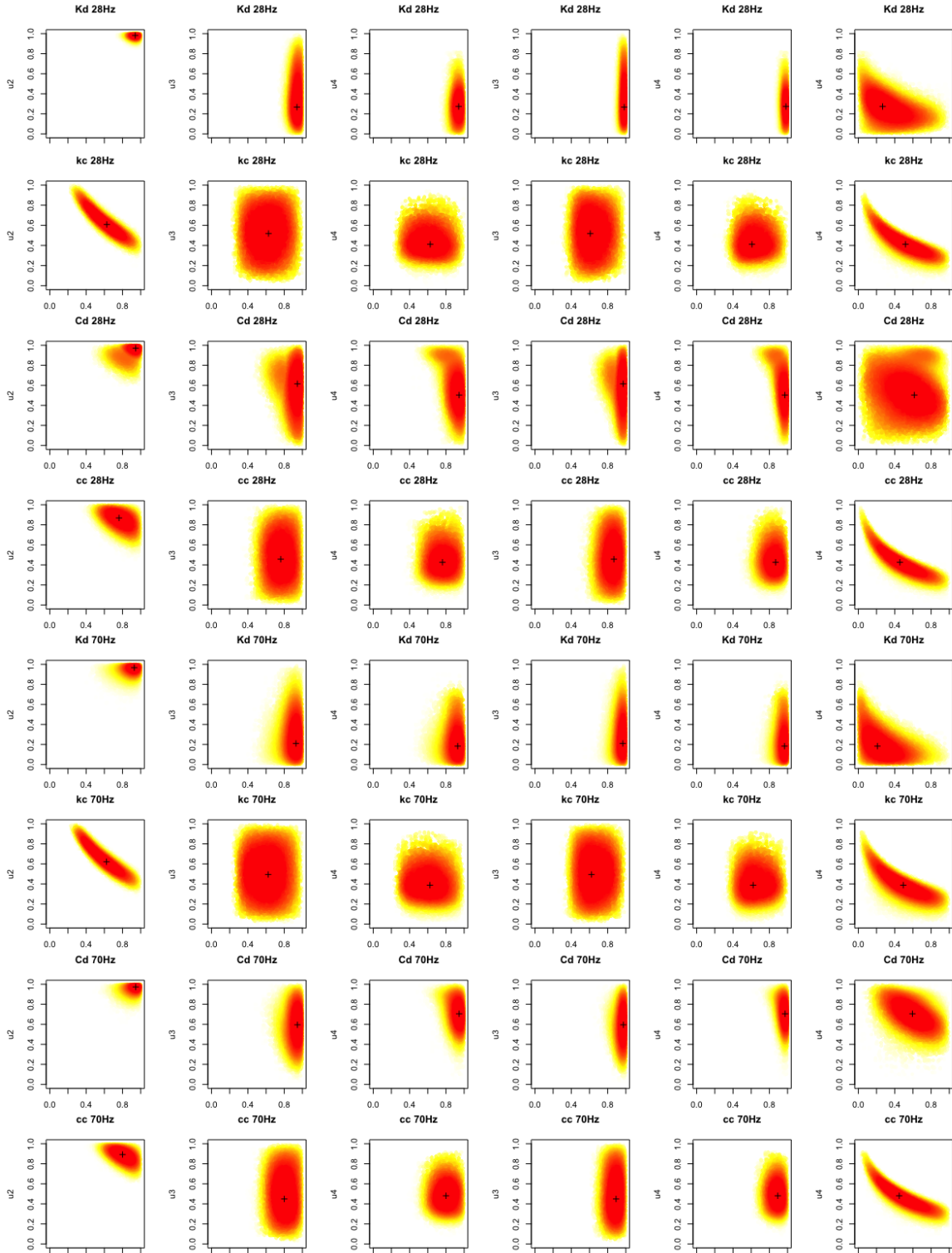


Figure 13: Bivariate marginals of single-output posterior samples of \mathbf{u} at 28 and 70 Hz.

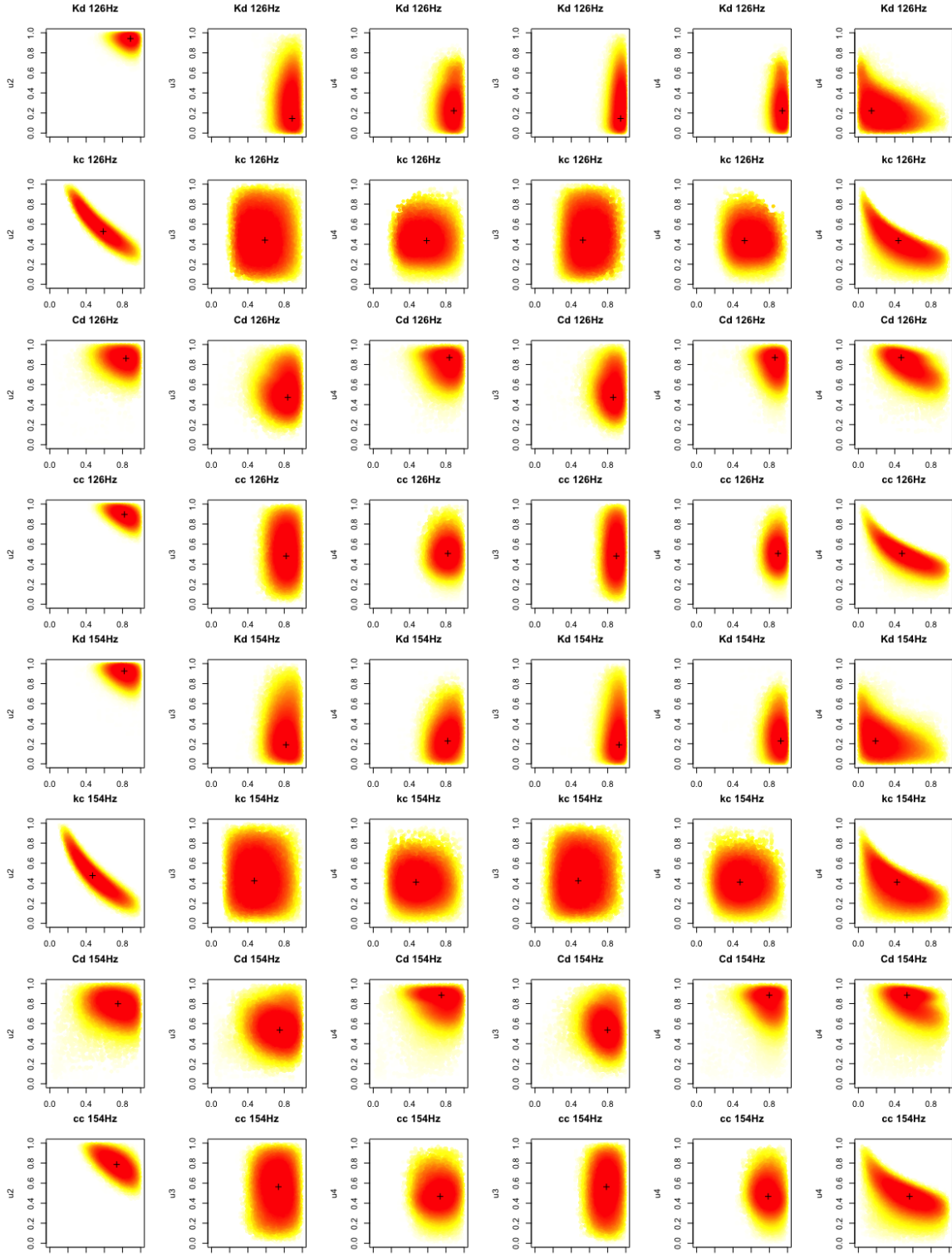


Figure 14: Bivariate marginals of single-output posterior samples of \mathbf{u} at 126 and 154 Hz.

A.2 PC-level calibration results: optimization and full Bayes

We display all 4 sets of PC-calibrated parameters \mathbf{u}_j^1 , for $j = 1, \dots, J$ using both modular optimization and fully Bayesian approaches developed from Section 4.2 in Figures 15 and 16. These are derived from 100,000 MCMC samples after burn-in. Optimization results are from 500 converged random multi-starts; “+” signs indicate the MAP values. To save space, we pair results from stiffness outputs, K_d and k_c , into Figure 15 and damping outputs, C_d and c_c , into Figure 16. All 4 outputs demonstrate distinct parameter distributions with varying levels of uncertainty. Stronger similarity can be observed between the damping outputs in Figure 16 than the stiffness ones in Figure 15. Compared with the fully integrated results in Figure 8, output cross stiffness k_c appears to be the most similar to the overall distribution.

A.3 Multiple-output OSSs prediction results

Here we complete multiple-output prediction and provided detailed notation and derivation for posterior prediction via multiple-output OSSs, described briefly in Section 6.

Augmenting Figure 10 from Section 6.1, we showcase LOO-CV in first-PCs for C_d and c_c in Figure 17. Contrasting with prediction without bias correction (blue), bias correction substantially reduces uncertainty in accuracy and enhances precision. Notice the bias term for C_d demonstrates a similar pattern as K_d , increasing generally as the observed output C_d increases. For output c_c , the bias correction term plays an even more crucial role for prediction when the computer model becomes noisy and less informative.

Figures 18–20 show LOO-CV means and 95% credible intervals in original outputs k_c , C_d , and c_c . These follow procedures described for K_d outputs shown in Figure 11 from Section 6.2, whose RMSEs are summarized numerically in Table 1.

Lastly, we detail the predictive mean and variance $(\mu_{j(\text{new})}^k, \Sigma_{j(\text{new})}^k)$ for new site location $\mathbf{x}_{(\text{new})}$ for the j th output property at frequency k as Eq. (21). Borrowing notation from

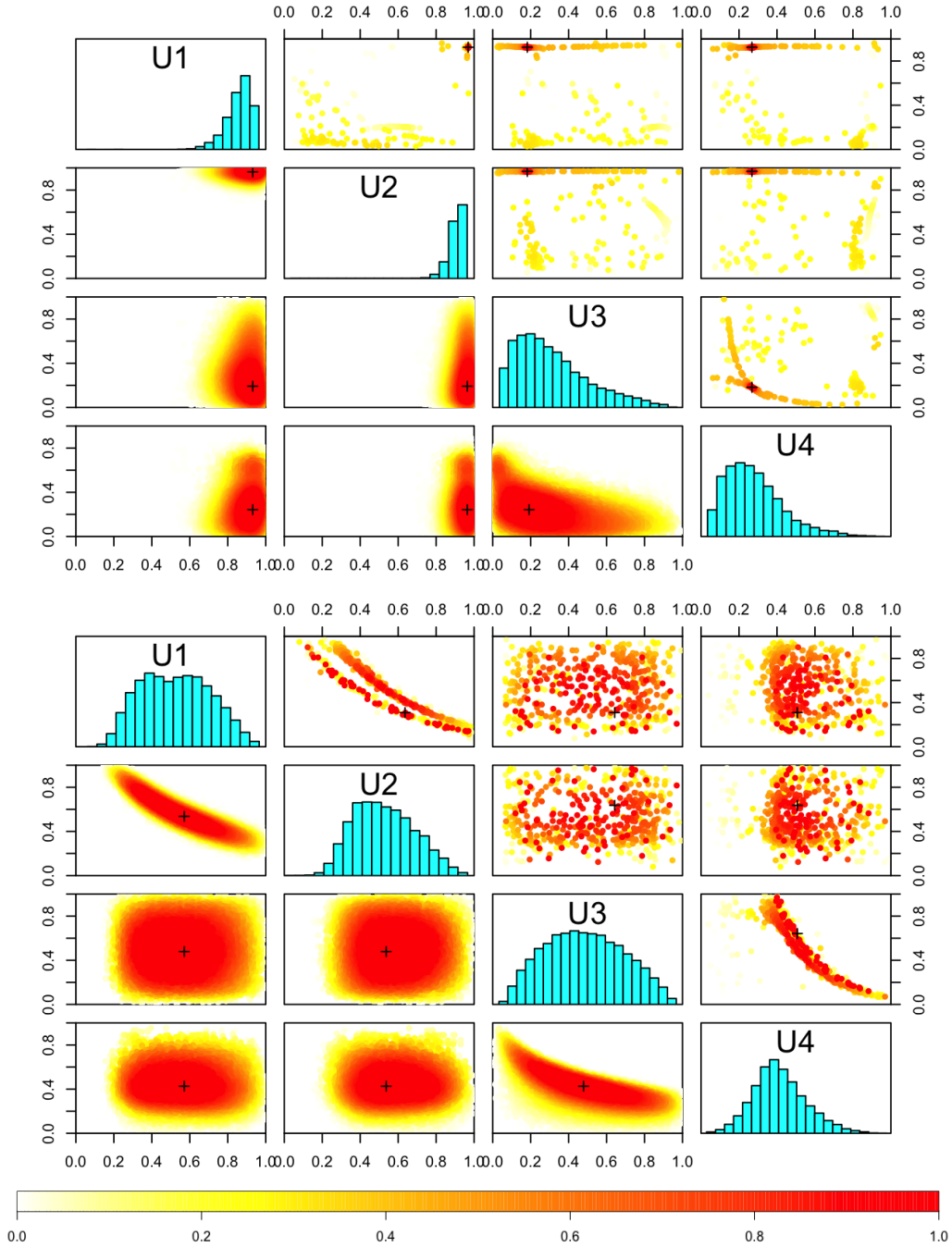


Figure 15: PC fully Bayesian (lower and diagonal) and modular optimization (upper) calibration results representing \mathbf{u}_1^1 for K_d (top) and \mathbf{u}_2^1 for k_c (bottom) combining 4 frequencies. Heat colors derived from rank of log posterior probability of these parameter values.

Eq. (2) but now in PC basis space, the joint distribution of the computer model training data $(\mathbf{X}_N, \mathbf{y}_j^{Mk})$, field training data $(\mathbf{X}_F, \mathbf{y}_j^{Fk})$, simulated size N' computer model data at

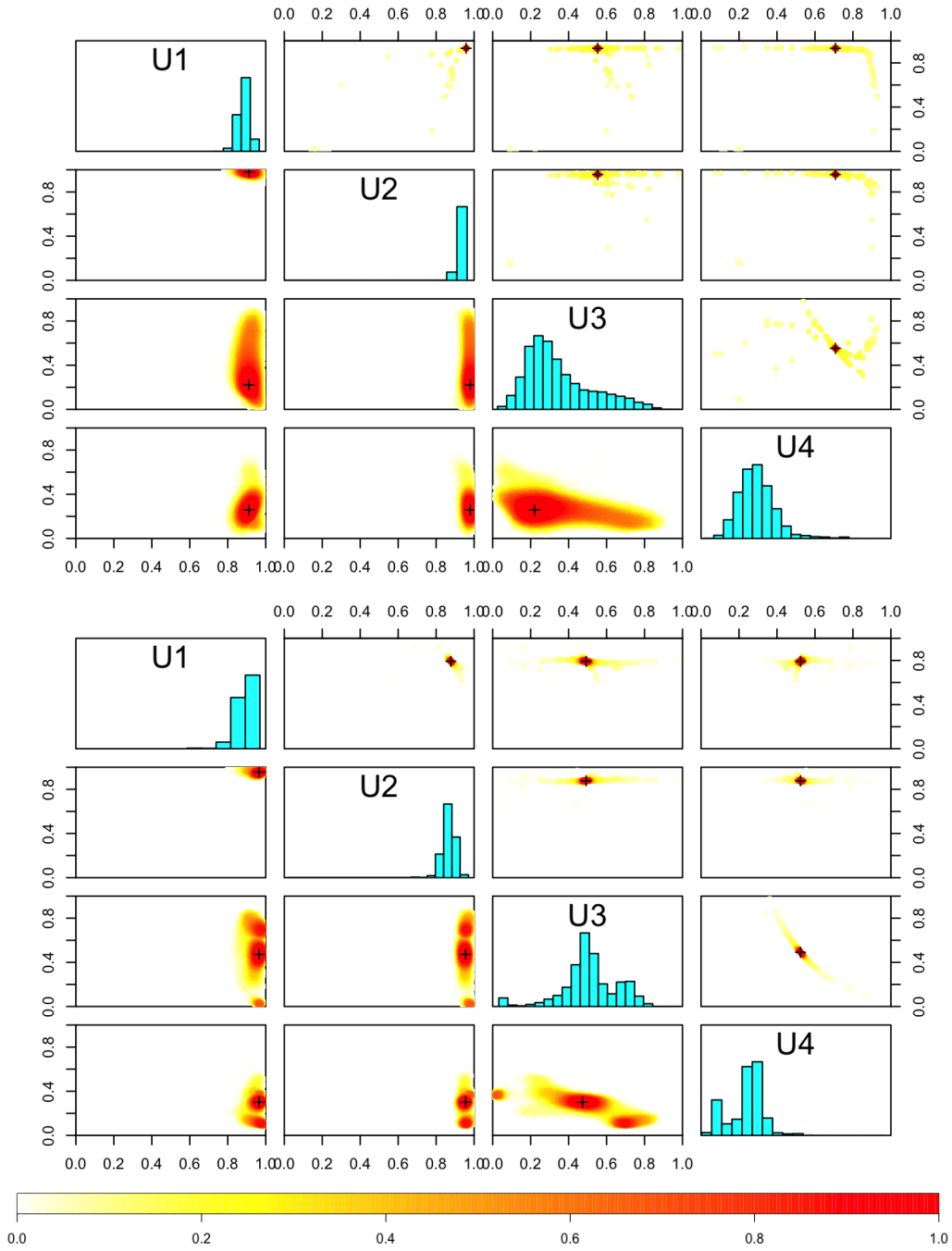


Figure 16: Similar to Figure 15 for C_d (top) c_c (bottom) combining 4 frequencies.

new site location $(\mathbf{x}_{(\text{new})}, \mathbf{y}_{j(\text{new})}^{Mk})$, and the unobserved field data of size F' at new location

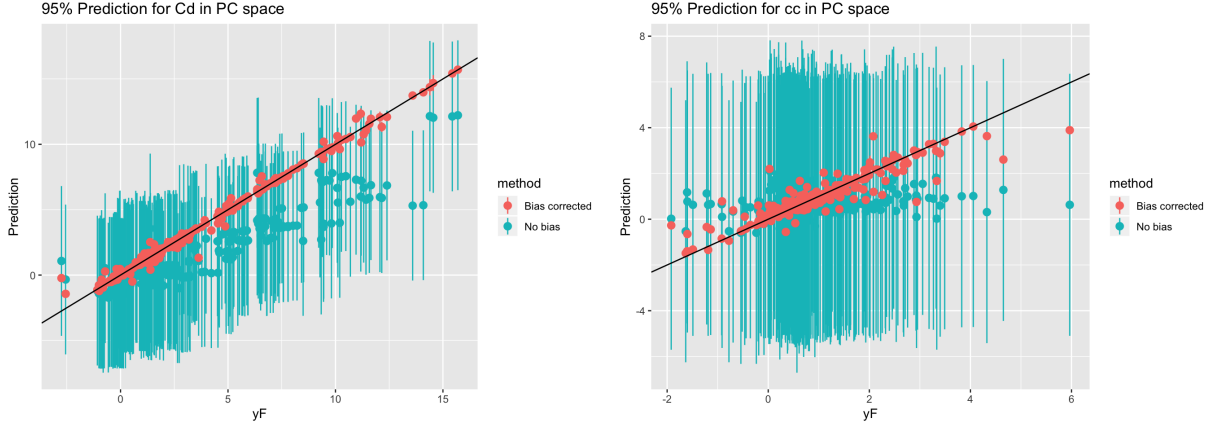


Figure 17: LOO-CV first-PC posterior predictive summaries for direct damping C_d and cross damping c_c . Intervals trace out 95%; black line has intercept zero, slope one.

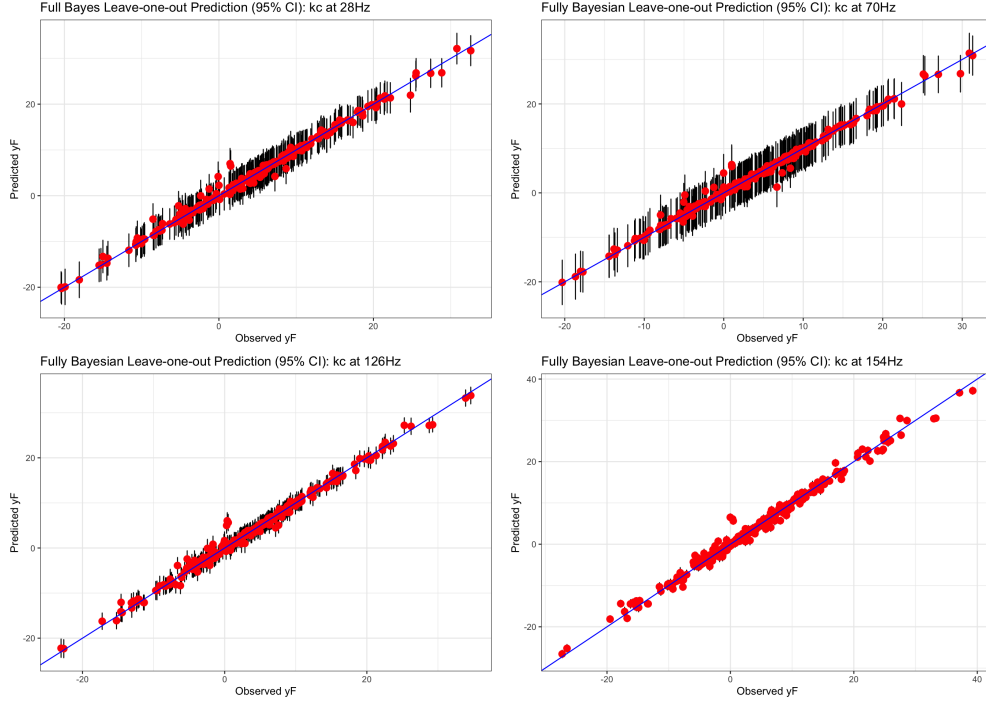


Figure 18: Cross stiffness k_c at 28, 70, 128, and 154 Hz; similar to Figure 11.

$(\mathbf{x}_{(\text{new})}, \mathbf{y}_{j(\text{new})}^{Fk})$ follows $(\mathbf{y}_j^{Mk}, \mathbf{y}_j^{Fk}, \mathbf{y}_{j(\text{new})}^{Mk}, \mathbf{y}_{j(\text{new})}^{Fk})^\top \sim \mathcal{N}(\mathbf{0}, \Sigma_P^{jk}(\mathbf{u}^1))$, where

$$\Sigma_P^{jk}(\mathbf{u}^1) \equiv \begin{bmatrix} \Sigma_N^{jk} & \Sigma_{F,N}^{jk}(\mathbf{u}^1)^\top & \mathbf{0} & \mathbf{0} \\ \Sigma_{F,N}^{jk}(\mathbf{u}^1) & \Sigma_F^{jk}(\mathbf{u}^1) + \Sigma_b^{jk} & \mathbf{0} & \Sigma_{F',F}^{jk\top} \\ \mathbf{0} & \mathbf{0} & \Sigma_{N'}^{jk(\text{new})} & \Sigma_{F',N'}^{jk(\text{new})}(\mathbf{u}^1)^\top \\ \mathbf{0} & \Sigma_{F',F}^{jk} & \Sigma_{F',N'}^{jk(\text{new})}(\mathbf{u}^1) & \Sigma_{F'}^{jk(\text{new})}(\mathbf{u}^1) + \Sigma_b^{jk(\text{new})} \end{bmatrix}. \quad (22)$$

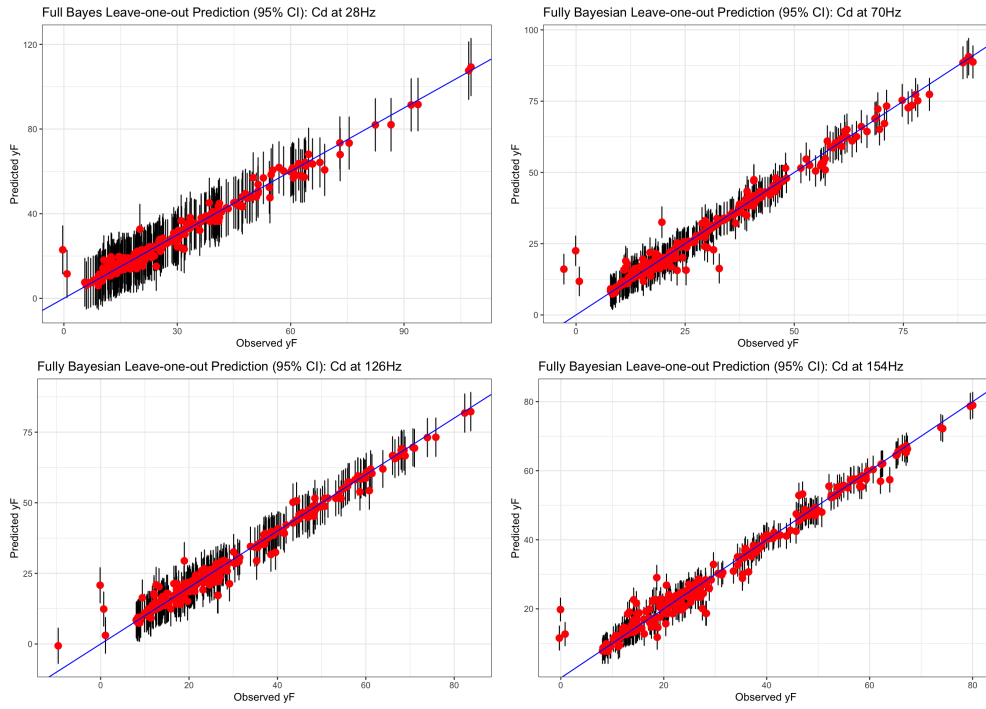


Figure 19: Direct damping C_d at at 28, 70, 128, and 154 Hz; similar to Figure 11.

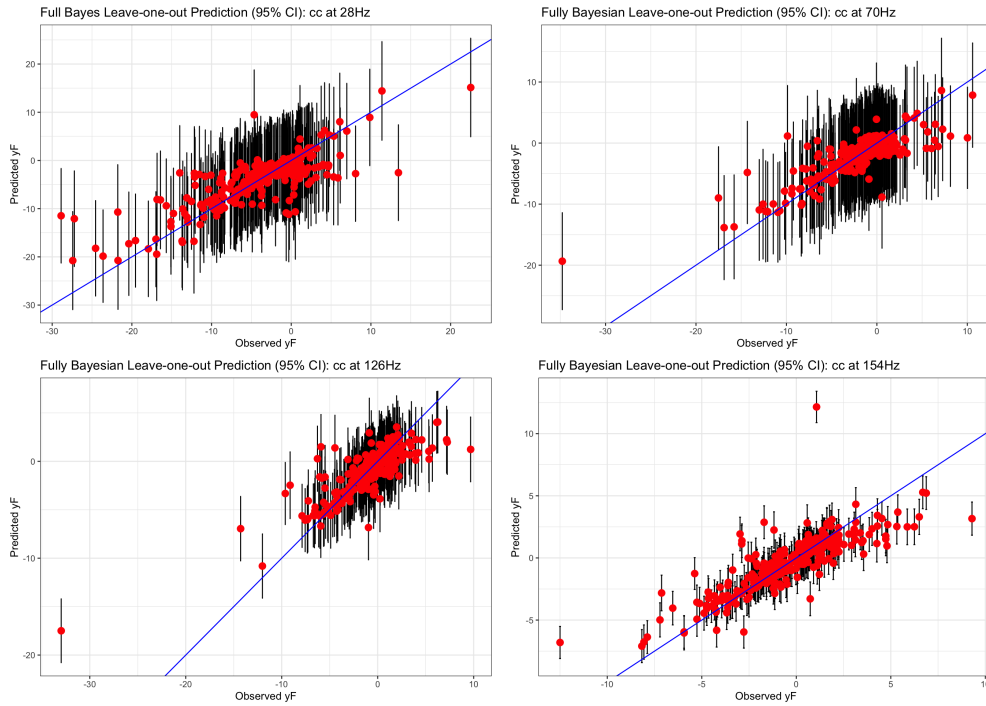


Figure 20: Cross damping c_c at at 28, 70, 128, and 154 Hz; similar to Figure 11.

In Eq. (22), multiple block-wise sparse structures are retained under multiple OSSs in all PC basis spaces. Following first-PC notation in from Eq. (16), $\Sigma_N^{jk} \equiv \text{Diag}[\Sigma_i^{jk}(\mathbf{U}_i, \mathbf{U}_i)]$, for $i = 1, \dots, F$, an upper-left block diagonal submatrix. Similarly, the off-diagonal $\Sigma_{F,N}^{jk}(\mathbf{u}^1)$ and field covariance $\Sigma_F^{jk}(\mathbf{u}^1) + \Sigma_b^{jk}$ follow. The covariance of the newly simulated computer model data are still block-diagonal, $\Sigma_N^{jk(\text{new})} \equiv \text{Diag}[\Sigma_i^{jk(\text{new})}(\mathbf{U}_i, \mathbf{U}_i)]$, for $i = F+1, \dots, F'$. Off-diagonal $\Sigma_{F,N}^{jk(\text{new})}(\mathbf{u}^1)$ and field covariance $\Sigma_F^{jk(\text{new})}(\mathbf{u}^1) + \Sigma_b^{jk(\text{new})}$ are analogous to training. Now, condition each new field observation $\mathbf{y}_{j(\text{new})}^{Fk}$ on the rest of all observed computer model data and field data in each of the PC bases,

$$(\mathbf{y}_{j(\text{new})}^{Fk} \mid \mathbf{y}_j^{Mk}, \mathbf{y}_j^{Fk}, \mathbf{y}_{j(\text{new})}^{Mk}, \Phi, \mathbf{u}^1) \sim \mathcal{N}(\mu_{j(\text{new})}^k, \Sigma_{j(\text{new})}^k), \quad j = 1, \dots, J, k = 1, \dots, K.$$

Following the joint covariance notation from Eq. (22), closed form predictive mean and variance $(\mu_{j(\text{new})}^k, \Sigma_{j(\text{new})}^k)$ for new site location $\mathbf{x}_{(\text{new})}$ are described in Eq. (21), in which $\mathbf{C}(\mathbf{u}^1) = \Sigma_F^{jk}(\mathbf{u}^1) + \Sigma_b^{jk} - \Sigma_{F,N}^{jk}(\mathbf{u}^1)(\Sigma_N^{jk})^{-1}\Sigma_{F,N}^{jk}(\mathbf{u}^1)^\top$.

A.4 Sensitivity analysis

To better understand the subtle relationship between calibration parameter prior settings, posterior and choices for discrepancy correction, we conducted a sensitivity analysis. For our motivating honeycomb example, we entertained three additional priors for calibration parameter \mathbf{u} beyond $(u_1, u_2, u_3, u_4) \stackrel{\text{iid}}{\sim} \text{Beta}(2, 2)$, which we refer to as the “regular” prior below. These new alternatives include: a “weak” adversarial prior $(u_1, u_2) \stackrel{\text{iid}}{\sim} \text{Beta}(1.5, 2.5)$ and $(u_3, u_4) \stackrel{\text{iid}}{\sim} \text{Beta}(2.5, 1.5)$, and a “prescient” prior with $(u_1, u_2) \stackrel{\text{iid}}{\sim} \text{Beta}(2.5, 1.5)$ and $(u_3, u_4) \stackrel{\text{iid}}{\sim} \text{Beta}(1.5, 2.5)$. Observe that the “weak” prior puts prior mass away from the MAP shown in Figure 8 where as the “prescient” one reinforces this setting. In addition to exploring how \mathbf{u} posteriors vary under these different prior settings, we consider a version without bias correction, “no bias” to contrast with “regular” prior. Two-dimensional

contour plots from all four scenarios have been overlaid in Figure 21.

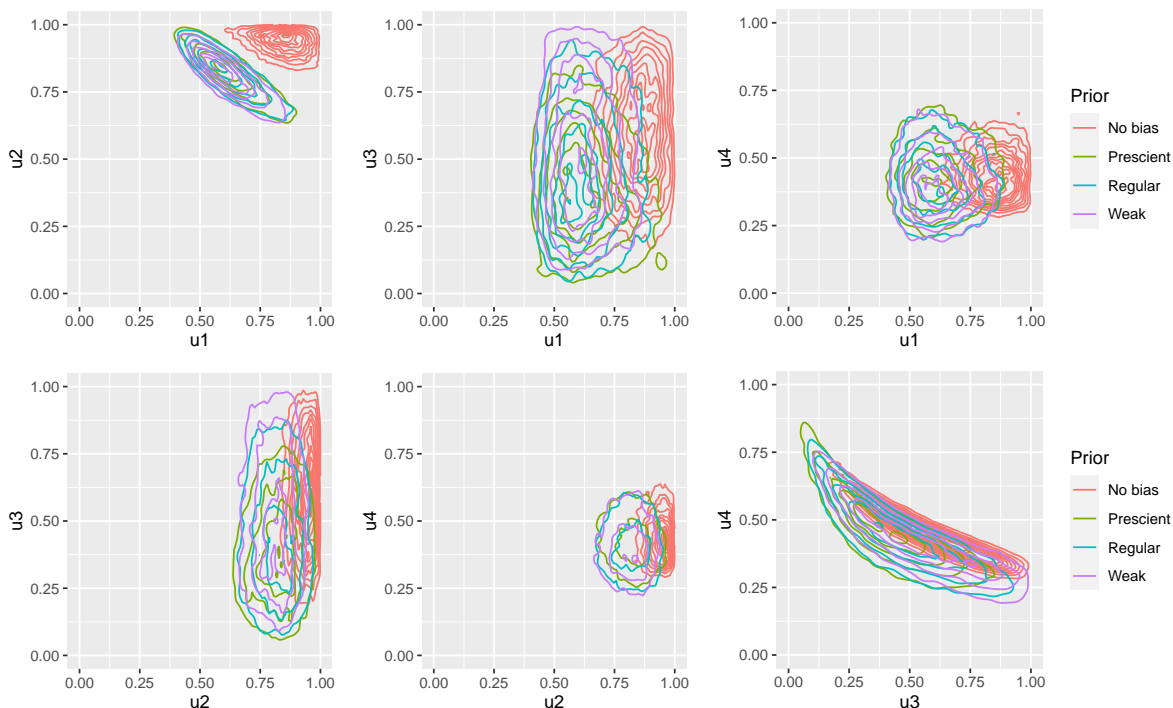


Figure 21: Bivariate marginal contour plots of 100,000 MCMC posterior samples of \mathbf{u} under: regular (cyan), weak (purple), and prescient (green) priors, and no bias correction (red).

Among all the three “bias corrected” prior settings, including regular (cyan), weak (purple), and prescient (green), observe that the posterior contours for \mathbf{u} largely overlap, suggesting that prior influence is weak relative to the likelihood (data influence), and that consequently our preferred analysis (“regular”) is robust in that sense. Taking a closer look at the middle plot in the first row and the left plot in the second row, the weak posterior (purple) contours encircle those of prescient posterior (green), demonstrating a meaningful and intuitive trend of impact from different prior choices on the posterior distributions. It is worth pointing out that these posteriors complement an analysis in (Huang et al., 2020) showing that a “uniform” prior on \mathbf{u} also works well, except mass is more concentrated on the boundaries of the input space where MAP is close to the end of the study region.

Now consider the “no bias” (red) posterior which is in sharp distinction, but also not altogether different. Only parameter pair (u_1, u_2) has shifted substantially, concentrating

on boundaries of their support. We already know that this setting leads to bad predictions (Figures 10 and 17, but perhaps this does not have a substantial effect on calibration.)